

A space-time smooth artificial viscosity method with wavelet noise indicator and shock collision scheme, Part 2: the 2- D case

Raaghav Ramani

Department of Mathematics
University of California
Davis, CA 95616 USA
rramani@math.ucdavis.edu

Jon Reisner

Los Alamos National Lab
XCP-4 MSF605
Los Alamos, NM 87544
reisner@lanl.gov

Steve Shkoller

Department of Mathematics
University of California
Davis, CA 95616 USA
shkoller@math.ucdavis.edu

March 3, 2022

Abstract

This is the second part to our companion paper [18]. Herein, we generalize to two space dimensions the C -method developed in [20, 18] for adding localized, space-time smooth artificial viscosity to nonlinear systems of conservation laws that propagate shock waves, rarefaction waves, and contact discontinuities. For gas dynamics, the C -method couples the Euler equations to scalar reaction-diffusion equations, which we call C -equations, whose solutions serve as space-time smooth artificial viscosity indicators for shocks and contacts.

We develop a high-order numerical algorithm for gas dynamics in 2- D which can accurately simulate the Rayleigh-Taylor (RT) instability with Kelvin-Helmholtz (KH) roll-up of the contact discontinuity, as well as shock collision and bounce-back. Solutions to our C -equations not only indicate the location of the shocks and contacts, but also track the geometry of the evolving fronts. This allows us to implement both directionally isotropic and anisotropic artificial viscosity schemes, the latter adding diffusion only in directions tangential to the evolving front. We additionally produce a novel shock collision indicator function, which naturally activates during shock collision, and then smoothly deactivates. Moreover, we implement a high-frequency 2- D wavelet-based noise detector together with an efficient and localized noise removal algorithm.

To test the methodology, we use a highly simplified WENO-based discretization scheme. We provide numerical results for some classical 2- D test problems, including the RT problem, the Noh problem, a circular explosion problem from the Liska & Wendroff [13] review paper, the Sedov blast wave problem, the double Mach 10 reflection test, and a shock-wall collision problem. In particular, we show that our artificial viscosity method can eliminate the wall-heating phenomenon for the Noh problem, and thereby produce an accurate, non-oscillatory solution, even though our simplified WENO-type scheme fails to run for this problem.

Contents

| | | |
|-----------|---|-----------|
| 1 | Introduction | 3 |
| 1.1 | Numerical discretization | 3 |
| 1.2 | Localization to shocks and contacts and capturing the geometry of the front | 4 |
| 1.3 | Shock collision and wavelet-based noise removal | 4 |
| 1.4 | Outline of the paper | 5 |
| 2 | The compressible Euler equations in 2-D | 5 |
| 3 | The C-method in the 2-D setting | 7 |
| 3.1 | Smoothly localizing the curves of discontinuity and tracking the geometry | 7 |
| 3.2 | The isotropic C -method and the Euler- C system | 8 |
| 4 | The anisotropic C-method for contact discontinuities | 9 |
| 4.1 | Calculating the normal and tangential directions to $\Gamma(t)$ | 10 |
| 4.2 | Directional artificial viscosity and the Euler- C^τ system | 12 |
| 5 | The C-method for shock-wall collision | 13 |
| 6 | A wavelet-based 2-D noise detection and removal algorithm | 14 |
| 6.1 | Construction of the highest frequency wavelets | 14 |
| 6.2 | Algorithm | 17 |
| 6.2.1 | Noise detection in the presence of discontinuities | 17 |
| 6.2.2 | Noise removal with a localized heat equation | 18 |
| 6.3 | Implementation of the algorithm for the Euler equations | 19 |
| 7 | The numerical algorithm for the C-method | 20 |
| 7.1 | Accuracy study: linear advection | 21 |
| 8 | The Noh infinite strength shock problem | 22 |
| 8.1 | Application of WENO- C - N to the Noh problem | 22 |
| 8.2 | Comparison with Noh's artificial viscosity scheme | 24 |
| 9 | The Sedov blast wave | 25 |
| 10 | The Sod circular explosion problem | 28 |
| 10.1 | The WENO- C - \hat{C} scheme applied to the Sod explosion problem | 28 |
| 10.2 | Shock-wall collision for a Sod-type explosion problem | 31 |
| 11 | The Mach 10 shock reflection problem | 32 |
| 12 | The Rayleigh-Taylor instability | 34 |
| 12.1 | Tangential spikes and the need for anisotropic diffusion | 36 |
| 12.1.1 | Boundary conditions for the RT problem | 38 |
| 12.2 | Application of WENO- C^τ - N to the RT instability | 38 |
| 12.2.1 | Comparison with isotropic artificial viscosity | 39 |
| 12.2.2 | Suppression of noise with the noise detection and removal algorithm | 41 |
| 13 | Concluding remarks | 45 |

| | |
|---|-----------|
| A Numerical discretization and schemes | 45 |
| A.1 WENO reconstruction procedure | 46 |
| A.2 The WENO- C and WENO- C - N schemes | 48 |
| A.3 The WENO- C^τ and WENO- C^τ - N schemes | 49 |
| A.4 Boundary conditions and ghost node values | 50 |
| A.4.1 Boundary conditions for the RT problem | 50 |

1 Introduction

This is the second in a two-part series of papers, in which we develop a high-order numerical algorithm, the C -method, to simulate compressible fluid flow with shock waves and contact discontinuities, as well as shock-wall collision and bounce-back. In the first part [18], we developed our scheme in one space dimension. This second part is devoted to the more geometric problem of simulating shocks, contacts, and collisions in two space dimensions.

Compressible fluid flow is an example of a system of nonlinear conservation laws, which in two space dimensions, can be written as

$$\begin{aligned}\partial_t \mathbf{U}(\mathbf{x}, t) + \partial_x \mathbf{F}(\mathbf{U}(\mathbf{x}, t)) + \partial_y \mathbf{G}(\mathbf{U}(\mathbf{x}, t)) &= \mathbf{0}, \\ \mathbf{U}(\mathbf{x}, t = 0) &= \mathbf{U}_0(\mathbf{x}),\end{aligned}$$

where $\mathbf{x} = (x, y)$ denotes coordinates on the plane, t denotes time, $\mathbf{U}(\mathbf{x}, t)$ is a vector of conserved quantities, and $\mathbf{F}(\mathbf{U})$ and $\mathbf{G}(\mathbf{U})$ denote the horizontal and vertical flux functions, respectively.

Even with smooth initial conditions, multi-dimensional conservation laws such as the compressible Euler equations develop singularities in finite-time [27, 4] and, in general, solutions consist of propagating shock waves and contact discontinuities. In two space dimensions, shocks and contacts produce *curves of discontinuities*, also known as *fronts*, which propagate according to the *Rankine-Hugoniot* conditions (see §2). The objective of a high-order numerical scheme is to produce a simulation which keeps the fronts sharp, while simultaneously providing high-order accuracy in smooth regions away from the front.

1.1 Numerical discretization

In §1.1 of [18], we described the tools necessary for designing high-order accurate numerical schemes in 1- D . In multi- D , similar tools are required to obtain non-oscillatory numerical schemes, but the multi-dimensional analogues are generally limited by mesh considerations. For structured grids (such as products of uniform 1- D grids), dimensional splitting is commonly used, decomposing the problem into a sequence of 1- D problems. This technique is quite successful, but stringent mesh requirements prohibits its use on complex domains. Moreover, applications to PDE outside of variants of the Euler equations may be somewhat limited. For further discussion of the limitations of dimensional splitting, we refer the reader to Crandall & Majda [6], and Jiang & Tadmor [9]. For unstructured grids, dimensional splitting is not available and alternative approaches must be employed, necessitated by the lack of multi- D Riemann solvers. WENO schemes on unstructured triangular grids have been

developed in Hu & Shu [7], but using simplified methods, which employ reduced characteristic decompositions, can lead to a loss of monotonicity and stability.

Algorithms that explicitly introduce diffusion provide a simple way to stabilize higher-order numerical schemes and subsequently remove non-physical oscillations near shocks. We refer the reader to the introductory sections in [20, 18] for a review of the classical artificial viscosity method [36].

In this paper, we develop a stable high-order 2- D numerical scheme that does not use approximate Riemann solvers or characteristic decompositions, but instead relies upon a 2- D generalization of the 1- D C -method [20, 18]. The extensive error analysis and convergence tests performed for the 1- D C -method in [18] indicate that the scheme is high order accurate. We expect that the 2- D implementation of the method presented in this paper is similarly high-order accurate, and we perform a number of numerical experiments to qualitatively support this claim. We also present error analysis and convergence studies for the Sedov problem to provide quantitative evidence for the claim of high order accuracy; further extensive convergence tests will be presented in [19].

1.2 Localization to shocks and contacts and capturing the geometry of the front

As we noted above, part one [18] provides a self-contained development of the 1- D C -method; for problems in one space dimension, the function $C(x, t)$ is the solution to a forced scalar reaction-diffusion equation, and serves as a highly localized space-time smooth indicator for the shock location. In 2- D , we again solve a scalar reaction-diffusion equation for $C(\mathbf{x}, t)$ on the plane; in this instance, the function $C(\mathbf{x}, t)$ not only serves as a localized indicator for both shocks and contacts, but is also able to accurately represent the geometry of the evolving fronts. Having this geometry allows us to define time-dependent normal and tangent vectors to the fronts, which, in turn, enables the construction of artificial viscosity methods that add diffusion only in certain directions rather than uniformly across the mesh. As we shall explain below, this type of anisotropic artificial viscosity scheme is essential in accurately capturing Kelvin-Helmholtz roll-up without overly diffusing the mixing regions in such flows.

1.3 Shock collision and wavelet-based noise removal

In part one [18], we consider the difficult problem of shock-wall collision and bounce-back in 1- D . In particular, when a shock wave collides with and reflects off of a fixed boundary, spurious oscillations develop behind the reflected shock. In addition to these post-collision oscillations, most schemes produce solutions that exhibit the phenomenon of anomalous *wall heating* [21]. A novel modification to the C -method in 1- D [18], wherein the time-dependent artificial viscosity parameter $\mathcal{B}(t)$ naturally increases during shock-wall collision and bounce-back, allows for the addition of extra “wall viscosity” to the shock front. This suppresses post-collision noise and the wall heating error, and ensures that the solution retains high-order accuracy away from the shock and prior to collision. In §5 of this paper, we present a generalization of the 1- D shock collision scheme to the 2- D setting, and apply the method to a circular explosion problem in §10.2.

The occurrence of high frequency noise in numerical solutions to PDE is a well-known issue. The first part of this work [18] provides a description of an efficient wavelet-based noise detection and heat equation-based noise removal algorithm for 1- D gas dynamics simulations. Error analysis and convergence tests in [18] show that the noise detection and removal algorithm decreases the errors of numerical solutions and improves the rate of convergence. In §6 of this paper, we present the natural extension of this 1- D algorithm to the 2- D case, with applications to the RT problem in §12 and the Noh problem in §8.

1.4 Outline of the paper

In §2, we introduce the 2- D compressible Euler equations and the Rankine-Hugoniot jump conditions relating the speed of propagation of curves of discontinuity with the jump discontinuities in the conservative variables. In §3, we present the *isotropic* C -method, and in §4, the *anisotropic* C -method, the latter designed for the long-time evolution of contact discontinuities. A new 2- D shock-wall collision scheme is introduced in §5, and a wavelet-based noise detection and *localized* heat equation-based noise removal procedure is developed in §6. Details about the numerical methods implemented are provided in §7 and Appendix A. We then apply the methods to a number of test problems. In particular, the C -method produces an accurate, non-oscillatory solution for the difficult Noh problem, whereas our simplified WENO-type algorithm (as well as more sophisticated advection schemes) fails to run for this problem.

2 The compressible Euler equations in 2- D

The compressible Euler equations in a 2- D rectangular domain $\Omega = (x_1, x_M) \times (y_1, y_N) \subset \mathbb{R}^2$ and a time interval $[0, T]$ are given in conservation law form as

$$\partial_t \mathbf{U}(\mathbf{x}, t) + \partial_x \mathbf{F}(\mathbf{U}(\mathbf{x}, t)) + \partial_y \mathbf{G}(\mathbf{U}(\mathbf{x}, t)) = \mathbf{0}, \quad \mathbf{x} \in \Omega, t > 0, \quad (1a)$$

$$\mathbf{U}(\mathbf{x}, 0) = \mathbf{U}_0(\mathbf{x}), \quad \mathbf{x} \in \Omega, t = 0, \quad (1b)$$

where the 4-vector $\mathbf{U}(\mathbf{x}, t)$ and the flux functions $\mathbf{F}(\mathbf{U})$ and $\mathbf{G}(\mathbf{U})$ are defined as

$$\mathbf{U} = \begin{pmatrix} \rho \\ \rho u \\ \rho v \\ E \end{pmatrix} \quad \text{and} \quad \mathbf{F}(\mathbf{U}) = \begin{pmatrix} \rho u \\ \rho u^2 + p \\ \rho uv \\ u(E + p) \end{pmatrix} \quad \text{and} \quad \mathbf{G}(\mathbf{U}) = \begin{pmatrix} \rho v \\ \rho uv \\ \rho v^2 + p \\ v(E + p) \end{pmatrix}.$$

Here, the vector $\mathbf{x} = (x, y)$ denotes the two Cartesian coordinates, ρ and E are the density and energy fields, respectively, u and v are the velocities in the x -direction and y -direction, respectively, and we use the notation \mathbf{u} to denote the velocity vector field $\mathbf{u} = (u, v)$. The pressure function p is defined by the equation of state

$$p = (\gamma - 1) \left(E - \frac{1}{2} \rho |\mathbf{u}|^2 \right), \quad (2)$$

where $|\mathbf{u}| = \sqrt{u^2 + v^2}$ and $\gamma > 1$ is the adiabatic constant. The system (1) represents the conservation of mass, momentum, and energy:

$$\partial_t \rho + \operatorname{div}(\rho \mathbf{u}) = 0, \quad \partial_t(\rho \mathbf{u}) + \operatorname{div}(\rho \mathbf{u} \otimes \mathbf{u}) + \nabla p = 0, \quad \partial_t E + \operatorname{div}((E + p)\mathbf{u}) = 0,$$

and defines a hyperbolic system, in the sense that both $\nabla \mathbf{F}$ and $\nabla \mathbf{G}$ have real eigenvalues; in particular, the four eigenvalues of $\nabla \mathbf{F}$ are

$$\lambda_1 = u - c, \quad \lambda_2 = \lambda_3 = u, \quad \lambda_4 = u + c,$$

and the four eigenvalues of $\nabla \mathbf{G}$ are

$$\lambda_5 = v - c, \quad \lambda_6 = \lambda_7 = v, \quad \lambda_8 = v + c.$$

The eigenvalues $\lambda_1, \lambda_5, \lambda_4$ and λ_8 correspond to sound waves, while the repeated eigenvalues $\lambda_2, \lambda_3, \lambda_6$, and λ_7 correspond to vorticity and entropy waves. We define the *maximum wave speed* $S(\mathbf{u})$ as

$$S(\mathbf{u}) = [S(\mathbf{u})](t) = \max_{i=1,\dots,8} \max_{\Omega} \{|\lambda_i(x, y, t)|\}. \quad (3)$$

We focus on solutions \mathbf{U} to the compressible Euler equations (1) that have a jump discontinuity across a time-dependent curve

$$\Gamma(t) = \cup_{i=1}^p \Gamma_i(t), \quad (4)$$

where for each index $i = 1, \dots, p$, $\Gamma_i(t)$ represents either a shock front or a contact discontinuity. In the case that $\Gamma_i(t)$ is a closed curve, we define $\mathbf{U}^+(x, t)$ to be the value of $\mathbf{U}(x, t)$ inside of $\Gamma_i(t)$ and $\mathbf{U}^-(x, t)$ to be the value of outside of $\Gamma_i(t)$. We then set

$$[\mathbf{U}]_{\pm}^{\pm} = \mathbf{U}^+ - \mathbf{U}^- \text{ at } \Gamma(t).$$

Let $\vec{n} = \vec{n}(x, y, t)$ and $\vec{\tau} = \vec{\tau}(x, y, t)$ be the unit normal and tangent vectors to $\Gamma(t)$, respectively. The Rankine-Hugoniot conditions relate the speed of propagation $\dot{\sigma}$ of the curve of discontinuity $\Gamma(t)$ with the jump discontinuity in the variables \mathbf{U} via the relation

$$\dot{\sigma}[\mathbf{U}]_{\pm}^{\pm} = [\mathbf{F} \cdot \vec{n}]_{\pm}^{\pm}.$$

If $\Gamma_i(t)$ is a shock,

$$[\mathbf{u} \cdot \vec{n}]_{\pm}^+ \neq 0 \text{ and } [\mathbf{u} \cdot \vec{\tau}]_{\pm}^+ = 0,$$

while if $\Gamma_i(t)$ is a contact discontinuity, then

$$[\mathbf{u} \cdot \vec{n}]_{\pm}^+ = 0 \text{ and } [\mathbf{u} \cdot \vec{\tau}]_{\pm}^+ \neq 0.$$

For the problems we consider in this paper, $[\rho]_{\pm}^+ \neq 0$ for both shocks and contacts.

3 The C -method in the 2- D setting

3.1 Smoothly localizing the curves of discontinuity and tracking the geometry

As noted above, the jump discontinuities of the density function describe the location of both the shock and contact fronts; as such, it is natural to use $|\nabla\rho(\mathbf{x}, t)|$ as an indicator for these time-dependent curves. Consequently, we track discontinuities by considering the quantity

$$G_\rho := \frac{|\nabla\rho|}{\max_\Omega |\nabla\rho|}. \quad (5)$$

We note that in the 1- D C -method formulation in [18], we use $|\partial_x u|$ instead of $|\partial_x \rho|$ as the forcing function for the C -equation. In 1- D , using either $|\partial_x u|$ or $|\partial_x \rho|$ as the forcing, together with the compression switch, produces identical results. In 2- D , the velocity is a vector quantity, whereas the density is a scalar function, so that the latter provides a simpler approach to tracking discontinuities.

In 2- D , we are interested in tracking both shock fronts and contact curves, and the density gradient provides a natural method for tracking both of these discontinuities. In Fig.1, we see that G_ρ captures both of the discontinuities, namely the shock front and the contact discontinuity, present in the solution.

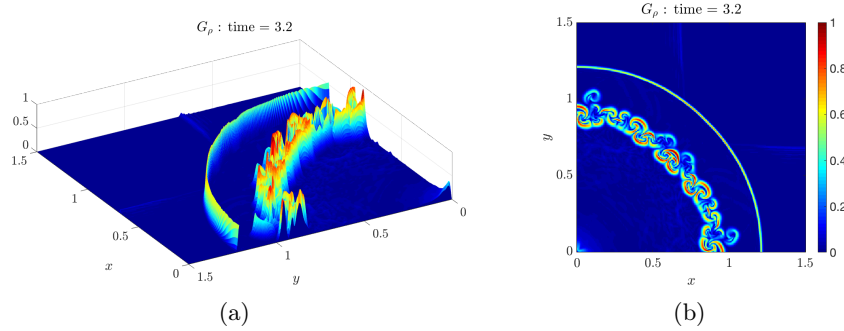


Figure 1: The function G_ρ for the Sod explosion problem at time $t = 3.2$.

Although the function G_ρ is able to localize artificial viscosity to a curve of discontinuity, its use in artificial viscosity operators often serves to produce an oscillatory solution [20, 18]. This is due to the rough nature of the localizing function G_ρ . Consequently, we first produce a space-time smooth variant of G_ρ through the use of the C -method. We describe the natural 2- D generalization of the 1- D C -equation as follows: we first define the operator \mathcal{L} as

$$\mathcal{L}[C; \varepsilon, \kappa] := -\frac{S(\mathbf{u})}{\varepsilon|\delta\mathbf{x}|}C + \kappa S(\mathbf{u})|\delta\mathbf{x}| \Delta C, \quad (6)$$

where $\delta\mathbf{x} = (\delta x, \delta y)$ with $\delta x, \delta y$ the grid spacings in the x and y directions, respectively, $S(\mathbf{u})$ is the maximum wave-speed (3), and $\Delta = \partial_{xx} + \partial_{yy}$ denotes the 2- D Laplace operator.

The space-time smooth version of G_ρ , which we denote by $C = C(\mathbf{x}, t)$, is the solution to the scalar linear parabolic PDE

$$\partial_t C(\mathbf{x}, t) - \mathcal{L}[C(\mathbf{x}, t); \varepsilon, \kappa] = \mathbb{1}_{\text{div} \mathbf{u} < 0} \frac{S(\mathbf{u})}{\varepsilon |\delta \mathbf{x}|} G_\rho(\mathbf{x}, t), \quad (7)$$

where the function $\mathbb{1}_{\text{div} \mathbf{u} < 0}$ is a *compression switch*¹ that ensures that C vanishes in regions of expansion, where there are no discontinuities in the solution. The parameters ε and κ in (6) control the support and smoothness of the solution C , respectively [20, 18].

The function $C(\mathbf{x}, t)$ provides not only the location of the shock and contact fronts, but also a good approximation to the geometry of the front. Specifically, the C function is sufficiently localized so as to provide the shape of the evolving front. In Fig.2, we show results of the evolution of a contact discontinuity associated to the Rayleigh-Taylor instability (which is discussed in §12). As can be seen, $|\nabla \rho|$ and hence the function G_ρ track the material interface accurately but the function G_ρ is very rough, particularly in directions tangential to the contact front. The function C , by contrast, is smooth and exhibits no oscillatory behavior, but is still highly localized to the contact discontinuity.

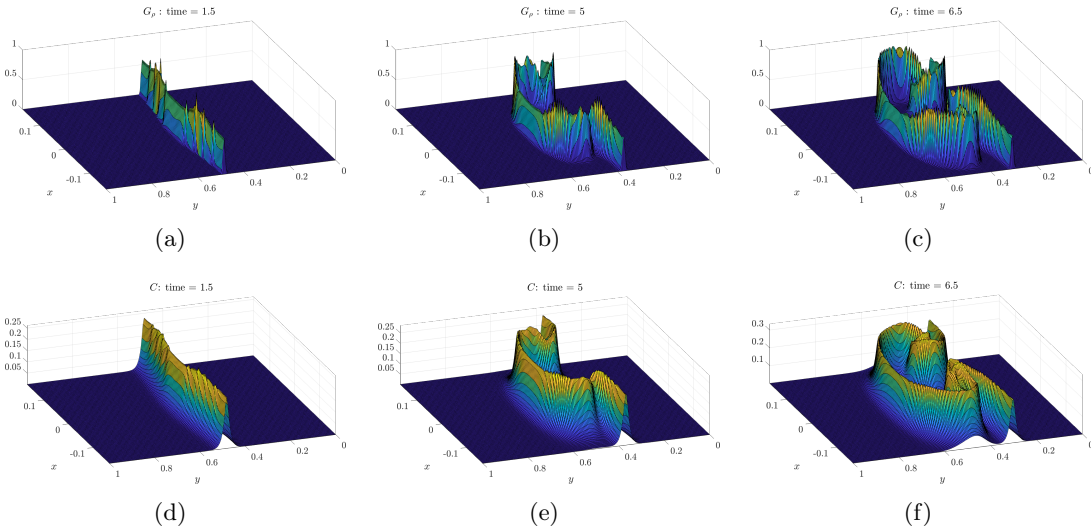


Figure 2: Comparison of G_ρ and C for the Rayleigh-Taylor instability at various times. The top row (a,b,c) are surface plots of G_ρ , and the bottom row (d,e,f) are surface plots of the corresponding C .

3.2 The isotropic C -method and the Euler- C system

We begin with a very natural generalization of the 1- D C -method to the 2- D setting. In particular, we first consider the 2- D Euler- C system with isotropic space-time smooth

¹ $\mathbb{1}_{\text{div} \mathbf{u} < 0}$ is equal to 1 on the set $\text{div} \mathbf{u} < 0$ and is equal to zero on $\text{div} \mathbf{u} \geq 0$.

artificial viscosity:

$$\partial_t \rho + \operatorname{div}(\rho \mathbf{u}) = 0, \quad (8a)$$

$$\partial_t(\rho u) + \partial_x(\rho u^2 + p) + \partial_y(\rho uv) = \operatorname{div} \left(\tilde{\beta}^u \rho C \nabla u \right), \quad (8b)$$

$$\partial_t(\rho v) + \partial_x(\rho uv) + \partial_y(\rho v^2 + p) = \operatorname{div} \left(\tilde{\beta}^v \rho C \nabla v \right), \quad (8c)$$

$$\partial_t E + \operatorname{div}(\mathbf{u}(E + p)) = \operatorname{div} \left(\tilde{\beta}^E \rho C \nabla (E/\rho) \right), \quad (8d)$$

$$\partial_t C - \mathcal{L}[C; \varepsilon, \kappa] = \mathbb{1}_{\operatorname{div} \mathbf{u} < 0} \frac{S(\mathbf{u})}{\varepsilon |\delta \mathbf{x}|} G_\rho, \quad (8e)$$

where the pressure p is given by the equation of state (2), $\mathcal{L} = \mathcal{L}[C; \varepsilon, \kappa]$ is the operator defined in (6), G_ρ is the forcing function defined in (5), and the artificial viscosity parameters are given by

$$\tilde{\beta}^{(\cdot)} := \frac{|\delta \mathbf{x}|^2}{\max_\Omega C} \beta^{(\cdot)}, \quad (9)$$

with $\beta^{(\cdot)}$ a constant.

We refer to the system (8) as the *isotropic* C -method, because artificial viscosity is added uniformly in all directions (although clearly still localized to the fronts via the use of C). We remark that the particular form of artificial viscosity used in the momentum equations (8b) and (8c) as well as the energy equation (8d) ensure that total energy remains conserved, and that E continues to evolve as the total energy function. For simplicity, suppose that periodic boundary conditions are enforced. On the one hand, integrating the energy equation (8d) yields $\frac{d}{dt} \int_\Omega E \, d\mathbf{x} = 0$. On the other hand, multiplying (8b) and (8c) by u and v , respectively, integrating over the domain Ω , summing the resulting quantities and utilizing the conservation of mass equation (8a), the energy equation (8d), and the equation of state (2) yields

$$\frac{d}{dt} \int_\Omega \frac{1}{2} \rho |\mathbf{u}|^2 + \frac{p}{\gamma - 1} \, d\mathbf{x} = 0.$$

This shows that the velocity \mathbf{u} and the pressure p adjust accordingly to maintain the relation (2), and that the Euler- C system conserves the total energy.

The space-time smooth localizing function C ensures that viscosity is added only at discontinuities, thereby ensuring that the solution retains high-order accuracy away from discontinuities, and, moreover, given that $C(\mathbf{x}, t)$ is a solution to a reaction-diffusion equation, it is smooth in both space and time. See [20] for the analysis of the solutions C .

4 The anisotropic C -method for contact discontinuities

We next consider the *anisotropic* C -method, specifically designed for the long-time evolution of contact discontinuities in the presence of Rayleigh-Taylor (RT) instabilities which lead to Kelvin-Helmholtz (KH) roll-up. We are particularly interested in the case that $[\rho]_-^+ \neq 0$ across the contact discontinuity², for which we also have that $[\mathbf{u} \cdot \vec{n}]_-^+ = 0$ and $[\mathbf{u} \cdot \vec{\tau}]_-^+ \neq 0$.

²KH instabilities can occur with a constant density profile, but we consider problems for which $[\rho]_-^+ \neq 0$. The method described here requires the condition $[\rho]_-^+ \neq 0$ to calculate the normal and tangent vectors to

Conservation of mass can be written as

$$\partial_t \rho + \mathbf{u} \cdot \nabla \rho = -\rho \operatorname{div} \mathbf{u},$$

and near an evolving front with tangent and normal vectors given by $\vec{\tau}$ and \vec{n} , respectively, the divergence of the velocity vector field \mathbf{u} is given by

$$\operatorname{div} \mathbf{u} = \partial_{\vec{\tau}} \mathbf{u} \cdot \vec{\tau} + \partial_{\vec{n}} \mathbf{u} \cdot \vec{n}.$$

Across a contact curve, $\partial_{\vec{n}} \mathbf{u} \cdot \vec{n}$ remains smooth, while $\partial_{\vec{\tau}} \mathbf{u} \cdot \vec{\tau}$ can become extremely oscillatory due to a combination of the discontinuity of $\mathbf{u} \cdot \vec{\tau}$ across the contact curve together with interpolation error of the contact curve onto a fixed grid (particularly in specifying the initial data). For simulations that require a great deal of time steps, it is important to add artificial viscosity in the tangential directions, but not in the normal directions.

In classical RT problems (and particularly for low Mach-number flows), instabilities that are generated by a small perturbation of the equilibrium interface position require a large number of time-steps to fully develop the KH roll-up of the contact curve, and it is most often the case that fluid mixing (due to numerical dissipation) is present in this roll-up region, so that the amplitude of the density and the gradient of the density can be significantly smaller than their maximum values.

The objective of our anisotropic C -method is to add diffusion only in directions that are tangent to the contact discontinuity, while adding no artificial diffusion in directions that are normal to the contact curve. In doing so, we can maintain a very sharp interface, and prevent over-diffusion of the slight “hills-and-valleys” which arise in the KH mixing zones. Moreover, when generating the RT instability of a small interface perturbation on a uniform rectangular grid (rather than using a velocity perturbation as done by ATHENA[29]), spurious *tangential spikes* can form in the velocity fields u and v along the contact curve; these spikes, in turn, generate small-scale numerical KH structures which contaminate the solution (this is discussed further in §12.1). Consequently, it is necessary to remove these spikes while maintaining a sharp interface; this may be accomplished through the use of anisotropic diffusion.

4.1 Calculating the normal and tangential directions to $\Gamma(t)$

The first task is to accurately compute a good approximation to the tangent vectors $\vec{\tau}$ to any curve of discontinuity $\Gamma(t)$, defined in (4). For the problems we consider here, this may be accomplished by setting

$$\tau_1(x, y, t) := \vec{\tau} \cdot \mathbf{e}_1 = -\partial_y \rho, \quad (10a)$$

$$\tau_2(x, y, t) := \vec{\tau} \cdot \mathbf{e}_2 = \partial_x \rho, \quad (10b)$$

where \mathbf{e}_1 and \mathbf{e}_2 denote the unit vectors in the x and y directions, respectively. In Fig.3, we provide vector plots of $\vec{\tau}$ calculated using (10), as well as surface plots of each component of

the evolving front. However, we remark that our algorithm can be adapted for problems for which $[\rho]_-^+ = 0$, and details are provided in the paper [19] under preparation.

$\vec{\tau}$, for the specific case of the RT instability³.

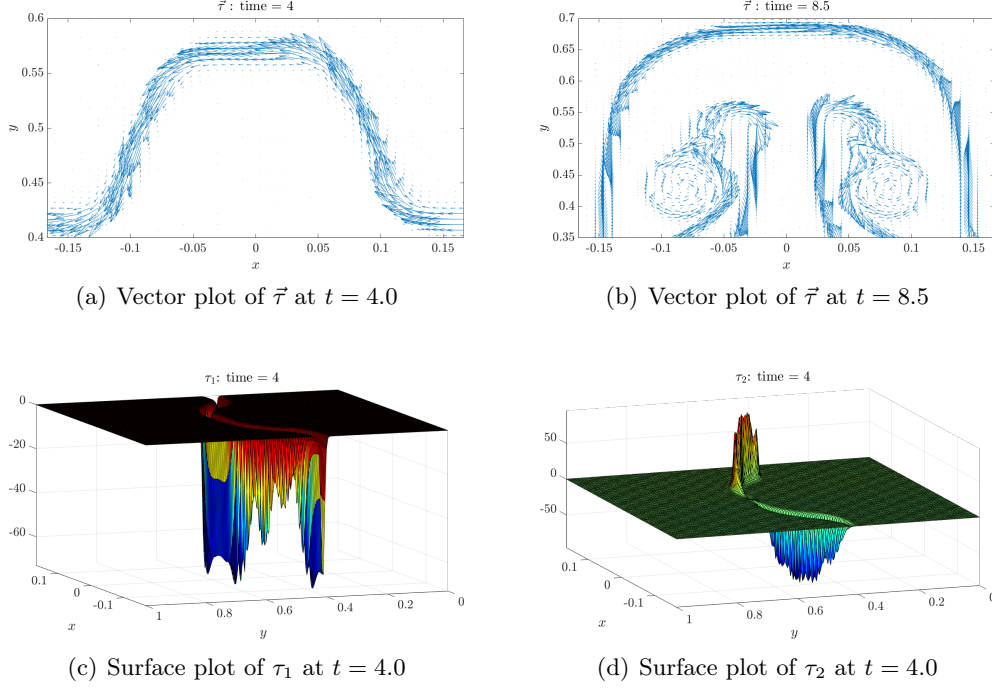


Figure 3: Calculation of the tangent vector $\vec{\tau}$ for the RT instability.

As shown in Fig.3, the functions τ_1 and τ_2 suffer from the same issue affecting the localizing function G_ρ ; namely, a lack of smoothness in both space and time. Consequently, we utilize the space-time smoothing mechanism provided by the C -method to produce regularized versions of τ_1 and τ_2 , which we denote C^{τ_1} and C^{τ_2} , respectively:

$$\partial_t C - \mathcal{L}[C^{\tau_1}; \varepsilon, \kappa] = \frac{S(\mathbf{u})}{\varepsilon|\delta\mathbf{x}|} \tau_1, \quad (11a)$$

$$\partial_t C - \mathcal{L}[C^{\tau_2}; \varepsilon, \kappa] = \frac{S(\mathbf{u})}{\varepsilon|\delta\mathbf{x}|} \tau_2, \quad (11b)$$

where \mathcal{L} is the operator defined in (6). We also define the function

$$\mu = \mu(t) := \max \{ \max \{ |C^{\tau_1}|, |C^{\tau_2}| \} \}, \quad (12)$$

which can be used to produce a “normalized” tangent vector $\frac{1}{\mu} \vec{C}^\tau = \frac{1}{\mu} C^{\tau_1} \mathbf{e}_1 + \frac{1}{\mu} C^{\tau_2} \mathbf{e}_2$.

³ We note that the vector plots in Figs.3(a) and 3(b) appear asymmetric only because of the Matlab plotting routine we use. In fact, for the RT problem we consider in this paper, the interface $\Gamma(t)$ is symmetric across the line $x = 0$. Since we fix an orientation for $\Gamma(t)$, the horizontal component of the tangent vector τ_1 is symmetric across $x = 0$, while the vertical component τ_2 is anti-symmetric, as can be seen in Figs.3(c) and 3(d). These facts, combined with the particular Matlab plotting routine we employ, cause the perceived asymmetry in the vector plots.

In Fig.4, we provide vector plots of the vector \vec{C}^τ , as well as surface plots of the components $\frac{1}{\mu}C^{\tau_1}$ and $\frac{1}{\mu}C^{\tau_2}$. These should be contrasted with the corresponding figures in Fig.3; we see that \vec{C}^τ is much smoother than $\vec{\tau}$, while remaining localized to the discontinuity $\Gamma(t)$.

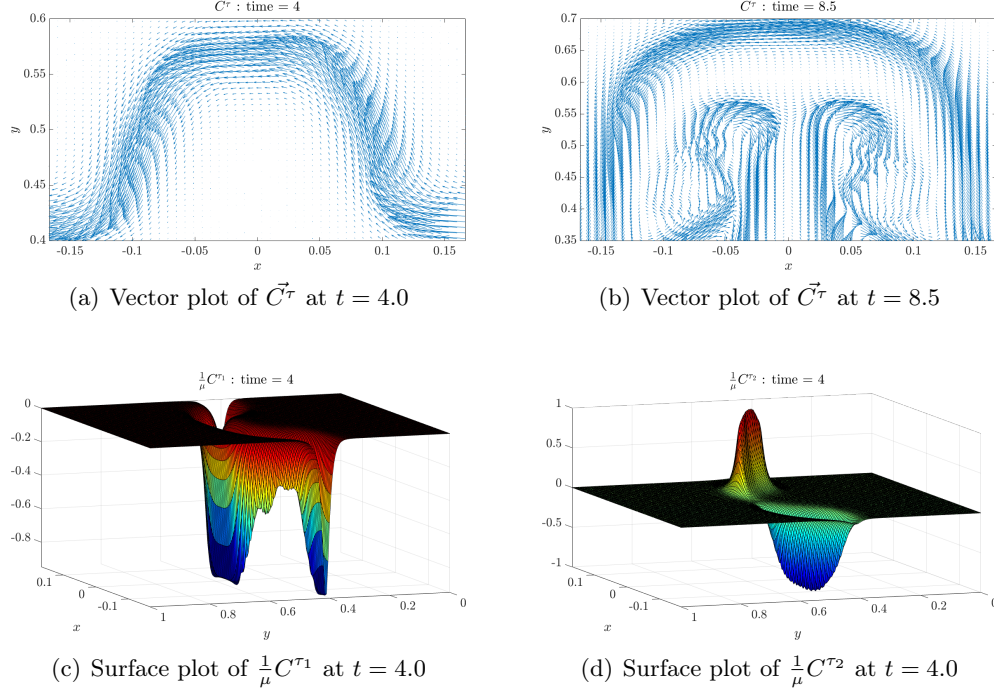


Figure 4: Calculation of the smoothed tangent vector \vec{C}^τ for the RT instability.

4.2 Directional artificial viscosity and the Euler- C^τ system

We now consider the following Euler- C^τ system for contact discontinuity evolution:

$$\partial_t \rho + \operatorname{div}(\rho \mathbf{u}) = 0, \quad (13a)$$

$$\partial_t(\rho u) + \partial_x(\rho u^2 + p) + \partial_y(\rho uv) = \partial_i \left(\tilde{\beta} \rho C^{\tau_i} C^{\tau_j} \partial_j u \right), \quad (13b)$$

$$\partial_t(\rho v) + \partial_x(\rho uv) + \partial_y(\rho v^2 + p) = \partial_i \left(\tilde{\beta} \rho C^{\tau_i} C^{\tau_j} \partial_j v \right), \quad (13c)$$

$$\partial_t E + \operatorname{div}(\mathbf{u}(E + p)) = 0, \quad (13d)$$

$$\partial_t C - \mathcal{L}[C; \varepsilon, \kappa] = \frac{S(\mathbf{u})}{\varepsilon |\delta \mathbf{x}|} G_\rho, \quad \partial_t C^{\tau_i} - \mathcal{L}[C^{\tau_i}; \varepsilon, \kappa] = \frac{S(\mathbf{u})}{\varepsilon |\delta \mathbf{x}|} \tau_i \text{ for } i = 1, 2, \quad (13e)$$

where G_ρ is given by (5), τ_1 and τ_2 by (10), \mathcal{L} by (6), and we utilize the Einstein summation convention, where a repeated free index in the same term implies summation over all values of

that index. We note that $\partial_1 \equiv \partial_x$ and $\partial_2 \equiv \partial_y$, and we use the two notations interchangeably. The artificial viscosity parameter is defined by

$$\tilde{\beta} = \frac{|\delta \mathbf{x}|^2}{\mu^2 \max_{\Omega} C} \beta, \quad (14)$$

with $\mu = \max_{\Omega} \{ \max \{ |C^{\tau_1}|, |C^{\tau_2}| \} \}$.

We note that the artificial viscosity operator $-\partial_i \left(\tilde{\beta} \rho C C^{\tau_i} C^{\tau_j} \partial_j \right)$ is a positive semi-definite operator. The proof is as follows: taking the scalar product of $-\partial_i \left(\tilde{\beta} \rho C C^{\tau_i} C^{\tau_j} \partial_j \mathbf{u} \right)$ with \mathbf{u} and integrating over Ω yields

$$\int_{\Omega} \tilde{\beta} \rho C C^{\tau_j} \partial_j \mathbf{u} \cdot C^{\tau_i} \partial_i \mathbf{u} \, d\mathbf{x} = \int_{\Omega} \tilde{\beta} \rho C |\partial_{\vec{C}^{\tau}} \mathbf{u}|^2 \, d\mathbf{x} \geq \tilde{\lambda} \int_{\Omega} |\partial_{\vec{C}^{\tau}} \mathbf{u}|^2 \, d\mathbf{x},$$

for some $\tilde{\lambda} \geq 0$. Here, $\partial_{\vec{C}^{\tau}} = \vec{C}^{\tau} \cdot \nabla$ denotes the smoothed tangential derivative operator. Thus, the anisotropic artificial viscosity operator is obtained as the Euler-Lagrange extremum associated to the function $\int \tilde{\beta} \rho C |\partial_{\vec{C}^{\tau}} \mathbf{u}|^2 \, d\mathbf{x}$. Just as in the case of isotropic artificial viscosity, our solutions to the Euler- C^{τ} system preserve total energy $E(t)$ (see §3.2).

5 The C -method for shock-wall collision

We now present a simple extension of the 1- D shock-wall collision scheme (see §3 [18]). Recall that the main novelty of the 1- D shock wall collision scheme is the use of a *wall function* $\overline{C}(t)$ which naturally activates during shock-wall collision and bounce-back. This allows for the addition of extra “wall viscosity” during shock-collision, which results in the suppression of post-collision noise while maintaining high-order accuracy prior to collision.

The natural generalization to the two-dimensional setting results in the 2- D Euler- C - W scheme:

$$\partial_t \rho + \operatorname{div}(\rho \mathbf{u}) = 0, \quad (15a)$$

$$\partial_t(\rho u) + \partial_x(\rho u^2 + p) + \partial_y(\rho uv) = \operatorname{div}(\mathcal{B}^u \rho C \nabla u), \quad (15b)$$

$$\partial_t(\rho v) + \partial_x(\rho uv) + \partial_y(\rho v^2 + p) = \operatorname{div}(\mathcal{B}^v \rho C \nabla v), \quad (15c)$$

$$\partial_t E + \operatorname{div}(\mathbf{u}(E + p)) = \operatorname{div}(\mathcal{B}^E \rho C \nabla(E/\rho)), \quad (15d)$$

$$\partial_t C - \mathcal{L}[C; \varepsilon, \kappa] = \mathbb{1}_{\operatorname{div} \mathbf{u} < 0} \frac{S(\mathbf{u})}{\varepsilon |\delta \mathbf{x}|} G_{\rho}, \quad (15e)$$

$$\partial_t C_w - \mathcal{L}[C_w; \varepsilon_w, \kappa_w] = \mathbb{1}_{\operatorname{div} \mathbf{u} < 0} \frac{S(\mathbf{u})}{\varepsilon_w |\delta \mathbf{x}|} G_{\rho}, \quad (15f)$$

where \mathcal{L} is the operator defined in (6), G_{ρ} is the forcing function defined in (5), and $\mathbb{1}_{\operatorname{div} \mathbf{u} < 0}$ is a compression switch. The artificial viscosity parameters \mathcal{B} are given by

$$\mathcal{B}^{(\cdot)} = \frac{|\delta \mathbf{x}|^2}{\max_{\Omega} C} \left(\beta^{(\cdot)} + \beta_w^{(\cdot)} \overline{C}(x, t) \right), \quad (16)$$

with the wall function $\bar{C}(x, t)$ defined by

$$\bar{C}(x, t) = \frac{C_w(x, y_l, t)}{\max_{\Omega} C_w(x, y, t)}.$$

Here, we assume that the shock-wall collision occurs at the bottom boundary $y = y_l$. A Neumann boundary condition for C_w is enforced at the bottom boundary $y = y_l$. As in the 1- D case, this results in the smooth growth in time of the amplitude of $\bar{C}(x, t)$ as the shock approaches the wall, and allows for the addition of “wall viscosity” during shock-wall collision and bounce-back.

6 A wavelet-based 2- D noise detection and removal algorithm

In this section, we extend the noise indicator algorithm presented in [18] to the two-dimensional setting, using the same ideas as in the 1- D case. Again, we construct a family of wavelets $\{\psi_{i,j}\}$ and obtain a set of wavelet coefficients $\{C_{i,j}\}$, found by calculating the inner product of the highest frequency wavelets with the noisy function. These wavelet coefficients will indicate the location of the noise, and we employ a localized heat equation-based solver to remove this noise.

6.1 Construction of the highest frequency wavelets

We first discretize our grid by assuming we have M cells in the x -direction, and N cells in the y -direction. Label the cell centers by (x_i, y_j) , where x_i and y_j are given by

$$\begin{aligned} x_i &= x_l + (i - 1) \cdot \delta x \quad \text{for } i = 1, \dots, M, \\ y_j &= y_l + (j - 1) \cdot \delta y \quad \text{for } j = 1, \dots, N, \end{aligned}$$

with $\delta x = (x_r - x_l)/(M - 1)$ and $\delta y = (y_r - y_l)/(N - 1)$. We group the cells into 3x3 blocks of 9 cells each, and then define the highest frequency wavelet with support over the domain spanned by the cell centers in each of these blocks, as shown in Fig.5.

This yields a set of $\frac{(M-1)}{2} \times \frac{(N-1)}{2}$ highest frequency wavelets. We denote these wavelets by $\psi_{i,j} = \psi_{i,j}(x, y)$, for $i = 1, \dots, (M - 1)/2$ and $j = 1, \dots, (N - 1)/2$, with each $\psi_{i,j}$ is supported in the rectangular domain $\mathcal{I}_{i,j} = [x_{2i-1}, x_{2i+1}] \times [y_{2j-1}, y_{2j+1}]$.

We now have to fix a form for the 2- D wavelet. The two key properties that are required of the wavelet family are:

1. Zero mean:

$$\int_{\Omega} \psi_{i,j}(\mathbf{x}) \, d\mathbf{x} = 0.$$

2. “Quasi-orthogonality” of the form:

$$\int_{\Omega} \psi_{i,j}(\mathbf{x}) \cdot \psi_{r,s}(\mathbf{x}) \, d\mathbf{x} = \delta_{ir} \delta_{js}, \quad \text{for } i, r = 1, \frac{M-1}{2} \text{ and } j, s = 1, \dots, \frac{N-1}{2},$$

so that each of the highest frequency wavelets is orthogonal to every other wavelet of the same frequency.

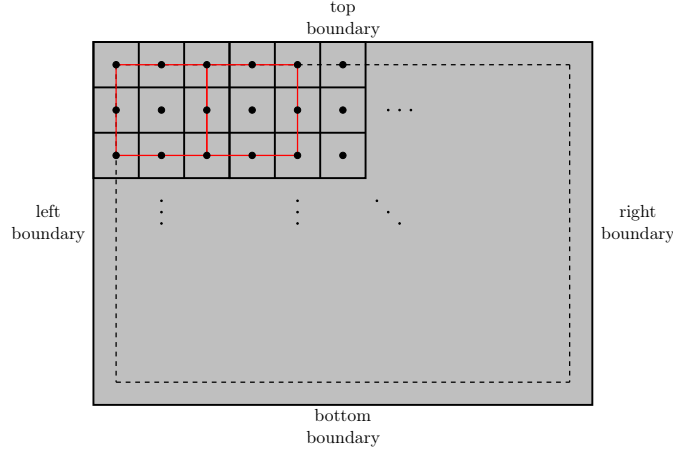


Figure 5: Grid setup for the construction of the wavelets in 2- D . The dashed black curve denotes the boundary $\partial\Omega$, while the solid black lines indicate cell edges. The black dots indicate cell centers, and the domains bounded by red lines indicate the support of each of the highest frequency wavelets.

We recall from [18] that each member of the 1- D wavelet family is oscillatory and orthogonal to all linear functions. Consequently, we design the 2- D wavelet family to also have these two properties. For simplicity, assume that a highest frequency wavelet ψ is supported in the domain $[-\delta x, \delta x] \times [-\delta y, \delta y]$. The highest frequency wavelets $\psi_{i,j}$ are then obtained by translation of ψ to the domain $\mathcal{I}_{i,j}$. Our wavelets take the form shown in Fig.6.

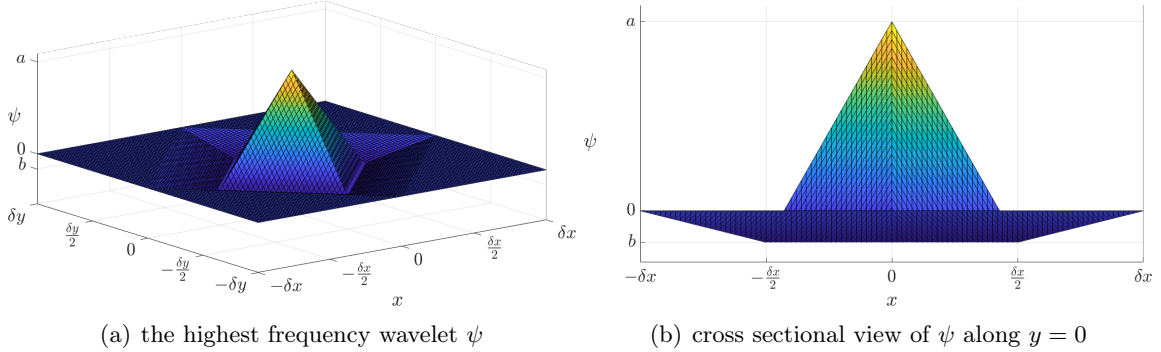


Figure 6: The highest frequency wavelet $\psi = \psi(x, y)$ in 2- D . We assume that the support of ψ is $\mathcal{I} = [-\delta x, \delta x] \times [-\delta y, \delta y]$.

The exact formula for the highest frequency wavelet ψ that is supported in the domain $\mathcal{I} = [-\delta x, \delta x] \times [-\delta y, \delta y]$ is

$$\psi(x, y) = \begin{cases} \psi^{(1)}(x, y), & \text{if } 0 \leq \left| \frac{x}{\delta x} \right| + \left| \frac{y}{\delta y} \right| \leq \frac{1}{2}, \\ \psi^{(2)}(x, y), & \text{if } \frac{1}{2} \leq \left| \frac{x}{\delta x} \right| + \left| \frac{y}{\delta y} \right| \leq 1, \end{cases}$$

where $\psi^{(1)}$ and $\psi^{(2)}$ are given by

$$\psi^{(1)}(x, y) = \begin{cases} a + 2(b - a) \left(\frac{x}{\delta x} + \frac{y}{\delta y} \right), & \text{if } x > 0, y > 0, \\ a + 2(b - a) \left(-\frac{x}{\delta x} + \frac{y}{\delta y} \right), & \text{if } x < 0, y > 0, \\ a + 2(b - a) \left(-\frac{x}{\delta x} - \frac{y}{\delta y} \right), & \text{if } x < 0, y < 0, \\ a + 2(b - a) \left(\frac{x}{\delta x} - \frac{y}{\delta y} \right), & \text{if } x > 0, y < 0, \end{cases}$$

$$\psi^{(2)}(x, y) = \begin{cases} 2b - 2b \left(\frac{x}{\delta x} + \frac{y}{\delta y} \right), & \text{if } x > 0, y > 0, \\ 2b - 2b \left(-\frac{x}{\delta x} + \frac{y}{\delta y} \right), & \text{if } x < 0, y > 0, \\ 2b - 2b \left(-\frac{x}{\delta x} - \frac{y}{\delta y} \right), & \text{if } x < 0, y < 0, \\ 2b - 2b \left(\frac{x}{\delta x} - \frac{y}{\delta y} \right), & \text{if } x > 0, y < 0. \end{cases}$$

Here, the values of a and b are chosen so that ψ satisfies $\|\psi\|_{L^2(\Omega)} = 1$ and the zero mean condition $\langle \psi, 1 \rangle_{L^2(\Omega)} = 0$, and can be calculated as

$$a = -6b \quad \text{and} \quad b = -\sqrt{\frac{3}{8}} \cdot \frac{1}{\delta x \delta y}.$$

The highest frequency wavelets $\psi_{i,j}$ are then obtained by translation of ψ to the domain $\mathcal{I}_{i,j} = [x_{2i-1}, x_{2i+1}] \times [y_{2j-1}, y_{2j+1}]$.

Now, given a function $f(x, y)$ defined at the cell centers (x_i, y_j) , we wish to calculate the inner product of f with each of the highest frequency wavelets. The first step is to approximate the function $f(x, y)$ over $\mathcal{I}_{i,j}$, the support of $\psi_{i,j}$. In 1- D , a function $f(x)$ is approximated as a piecewise linear function over the interval \mathcal{I}_i , the support of a 1- D highest frequency wavelet, by linearly interpolating between the cell center values (see §4 in [18]). The analogue of a line in the two-dimensional setting is a plane, so a first attempt is to approximate $f(x, y)$ by a plane in each of the sub-cells $[x_r, x_{r+1}] \times [y_s, y_{s+1}]$. However, this is not possible, since 3 points define a plane, whereas each of the sub-cells contains 4 cell center values.

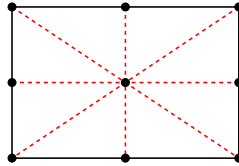


Figure 7: Dividing $\mathcal{I}_{i,j}$ into 8 regions.

Our solution is to divide $\mathcal{I}_{i,j}$ into 8 regions as shown in Fig.7. Each of these regions contains precisely 3 cell-center values, and these 3 values define a plane. Thus, we can approximate $f(x, y)$ by a plane in each of these 8 regions, and define a piecewise linear function $\tilde{f}(x, y)$ such that $\tilde{f}(x_i, y_j) = f(x_i, y_j)$. We may then approximate the (i, j) -th wavelet coefficient as

$$\begin{aligned} \mathcal{C}_{i,j}(f) &:= \langle f, \psi_{i,j} \rangle_{L^2(\Omega)} \approx \langle \tilde{f}, \psi_{i,j} \rangle_{L^2(\Omega)} \\ &= -\frac{\sqrt{6} \delta x \delta y}{192} \left\{ \begin{array}{cccc} f_{2i-1,2j+1} & + & 2f_{2i,2j+1} & + & f_{2i+1,2j+1} & + \\ 2f_{2i-1,2j} & + & -12f_{2i,2j} & + & 2f_{2i+1,2j} & + \\ f_{2i-1,2j-1} & + & 2f_{2i,2j-1} & + & f_{2i+1,2j-1} & \end{array} \right\}, \end{aligned} \quad (17)$$

where $f_{m,n} = f(x_m, y_n)$. One can verify that the inner product of $\psi_{i,j}$ with an arbitrary plane is identically zero i.e. if $f(x, y) = \alpha x + \beta y$ for some constants α and β , then $\mathcal{C}_{i,j}(u) = 0$ for every $i = 1, \dots, (M-1)/2$ and $j = 1, \dots, (N-1)/2$. This is analogous to the result in 1- D that each of the highest frequency wavelets is orthogonal to linear functions.

6.2 Algorithm

Given a noisy function $\tilde{u}(x, y)$, we now present an algorithm for first detecting and then subsequently removing the noise. The algorithm is almost identical to that presented for the 1- D case (see §4 in [18]).

6.2.1 Noise detection in the presence of discontinuities

We first calculate, using formula (17), the $\frac{M-1}{2} \times \frac{N-1}{2}$ wavelet coefficients, each associated with one of the highest frequency wavelets. The coefficients that are largest in magnitude should indicate the location of the noise. However, as in the 1- D case, it is possible that the wavelet coefficients that are largest in magnitude are actually indicating the location of the curve of discontinuity $\Gamma(t)$. Since the C -method is taking care of artificial diffusion in this region, one needs to manually “turn off” the noise detection in a small region surrounding the shock curve $\Gamma(t)$. There are numerous ways to do this, but we employ one of the simplest methods, namely to turn off the noise detection if

$$\frac{C}{\max_{\Omega} C} > \delta_{\text{off}}, \quad (18)$$

where δ_{off} is some value between 0 and 1. A typical range of values for δ_{off} is $\delta_{\text{off}} \in [0.05, 0.25]$.

With noise detection deactivated in the region surrounding $\Gamma(t)$, the wavelet coefficients that are largest in magnitude now indicate the location of the noise. We now “turn on” a noise detector function $\mathbb{1}_{\text{noise}}(x, y)$ in the domain $\mathcal{I}_{i,j}$ if the associated wavelet coefficient $\mathcal{C}_{i,j}$ satisfies $|\mathcal{C}_{i,j}| \geq C_{\text{ref}}$. The constant C_{ref} is the wavelet coefficient obtained from a “typical” high-frequency oscillation, namely a hat function (see Fig.8) centered in the domain

$[-\delta x, +\delta x] \times [-\delta y, +\delta y]$ with amplitude δh . The associated wavelet coefficient may then be calculated as

$$c_{\text{ref}} = \delta h \frac{\sqrt{6 \delta x \delta y}}{16}. \quad (19)$$

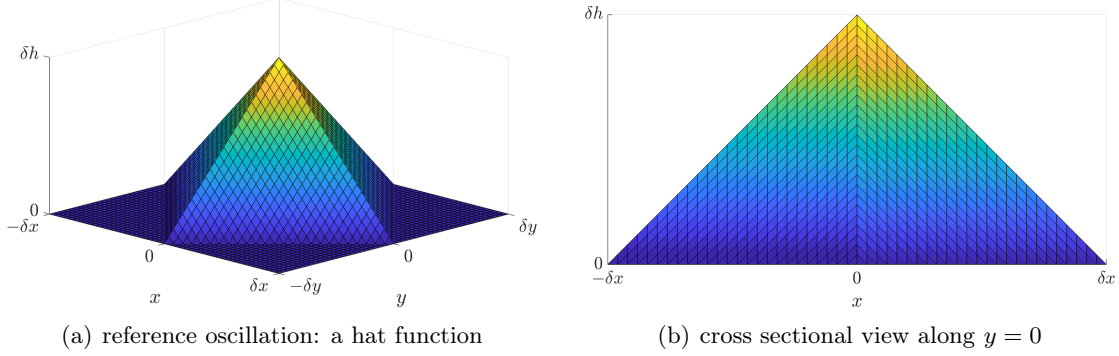


Figure 8: The 2- D reference oscillation: a hat function with amplitude δh .

6.2.2 Noise removal with a localized heat equation

The noise removal process in the 2- D case is identical to that in 1- D . We first construct the domain \mathcal{V} , given by the union of all domains $\mathcal{I}_{i,j}$ such that the noise detector function $\mathbb{1}_{\text{noise}}(x, y)$ is non-zero in $\mathcal{I}_{i,j}$. We write \mathcal{V} as the union of its connected subsets $\mathcal{V} = \bigcup_k \mathcal{V}_k$, and then define the domains $\tilde{\mathcal{V}}_k$ as the domain \mathcal{V}_k extended by one cell in each outward in each direction (see Fig.9). For example, if $\mathcal{V}_k = [x_1, x_2] \times [y_1, y_2]$, then $\tilde{\mathcal{V}}_k = [x_1 - \delta x, x_2 + \delta x] \times [y_1 - \delta y, y_2 + \delta y]$.

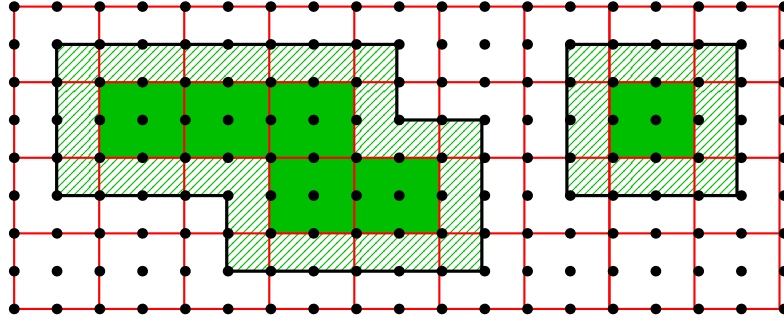


Figure 9: Construction of the domains \mathcal{V}_k and $\tilde{\mathcal{V}}_k$. The squares bounded by the red lines indicate the support of each of the highest frequency wavelets $\psi_{i,j}$. The shaded green regions indicate where the noise indicator algorithm detects noise, and represent the domains \mathcal{V}_k . The hatched regions indicate the extension of each \mathcal{V}_k to $\tilde{\mathcal{V}}_k$. The domains $\tilde{\mathcal{V}}_k$ are the regions bounded by the solid black lines.

A localized heat equation with Dirichlet boundary conditions is then solved in each of

the domains $\tilde{\mathcal{V}}_k$ for a “de-noised” solution $u(x, y, \tau)$,

$$\partial_\tau u(x, y, \tau) = \eta \cdot \Delta u(x, y, \tau), \quad \text{for } \mathbf{x} \in \tilde{\mathcal{V}}_k \text{ and } \tau > 0, \quad (20a)$$

$$u(x, y, 0) = \tilde{u}(x, y), \quad \text{for } \mathbf{x} \in \tilde{\mathcal{V}}_k, \quad (20b)$$

$$u(x, y, \tau) = \tilde{u}(x, y), \quad \text{for } \mathbf{x} \in \partial\tilde{\mathcal{V}}_k \text{ and } \tau > 0, \quad (20c)$$

while $u(x, y, \tau) = \tilde{u}(x, y)$ for $\mathbf{x} \in \left(\bigcup_k \tilde{\mathcal{V}}_k\right)^c$ and $\tau \geq 0$. The time τ is a fictitious time, introduced solely for the diffusion mechanism, while $0 < \eta \ll 1$ is a small constant, which we refer to as the noise removal viscosity. Equation (20b) is the initial condition, and (20c) is a Dirichlet boundary condition ensuring continuity of $u(x, y, \tau)$ over the domain Ω .

However, as in the 1- D case, it is not necessary to explicitly construct the domains $\tilde{\mathcal{V}}_k$. Instead, one can use the noise detector function $\mathbb{1}_{\text{noise}}(x, y)$ and solve a modified heat equation with Dirichlet boundary conditions, given by

$$\partial_\tau u(x, y, \tau) = \eta \cdot \mathbb{1}_{\text{noise}}(x, y) \cdot \Delta u(x, y, \tau), \quad \text{for } \mathbf{x} \in \Omega \text{ and } \tau > 0, \quad (21a)$$

$$u(x, y, 0) = \tilde{u}(x, y), \quad \text{for } \mathbf{x} \in \Omega, \quad (21b)$$

$$u(x, y, \tau) = \tilde{u}(x, y), \quad \text{for } \mathbf{x} \in \partial\Omega \text{ and } \tau > 0. \quad (21c)$$

In practice, the system (21) is solved using a simple, explicit forward Euler time integration scheme, along with a second order central difference approximation for the spatial derivatives. Moreover, in the simulations shown below, a single time-step is sufficient to remove noise; thus, our procedure is the equivalent of the inversion of a Helmholtz elliptic operator, and can hence be viewed as a *filtering* process, in which high frequency noise is eliminated from the solution through a local averaging or localized frequency truncation. However, we remark that for certain simulations with very large amplitude high frequency noise, it may be necessary to solve the localized heat equation for several time steps to completely remove the oscillations.

6.3 Implementation of the algorithm for the Euler equations

We now describe how we implement the noise detection and removal algorithm described above for the particular case of the Euler system (1). Suppose that we are given the solution $\mathbf{U} = \mathbf{U}(x, y, t_n)$ at time $t = t_n = n \cdot \delta t$, and we wish to calculate the solution $\mathbf{U}(x, y, t_{n+1})$ at time $t = t_{n+1} = (n + 1) \cdot \delta t$. The implementation proceeds in two steps:

1. We first compute in the usual manner the (potentially noisy) solution at time $t = t_{n+1}$. We denote this solution by $\tilde{\mathbf{U}}(x, y)$. In the numerical studies below, a simplified WENO-based scheme for the spatial discretization and an explicit Runge-Kutta method for the time integration are used to calculate this solution.
2. We then pass the potentially noisy velocity components $\tilde{u}(x, y)$ and $\tilde{v}(x, y)$ through the noise detection and removal algorithm described in §6.2, to produce de-noised velocity components $u(x, y, t_{n+1})$ and $v(x, y, t_{n+1})$. We then *define* the solution $\mathbf{U}(x, y, t_{n+1})$

at time $t = t_{n+1}$ by

$$U(x, y, t_{n+1}) \equiv \begin{bmatrix} \rho(x, y, t_{n+1}) \\ \rho u(x, y, t_{n+1}) \\ \rho v(x, y, t_{n+1}) \\ E(x, y, t_{n+1}) \end{bmatrix} := \begin{bmatrix} \tilde{\rho}(x, y) \\ \tilde{\rho}(x, y) \cdot u(x, y, t_{n+1}) \\ \tilde{\rho}(x, y) \cdot v(x, y, t_{n+1}) \\ \tilde{E}(x, y) \end{bmatrix}.$$

This algorithm mimics the 1- D version in [18]. We apply this procedure to the Rayleigh-Taylor instability in §12 and demonstrate its ability to suppress spurious high frequency noise that otherwise corrupts the solution.

REMARK 1. We note that the noise removal procedure for the horizontal velocity component \tilde{u} is completely independent from the noise removal procedure for the vertical velocity component \tilde{v} . It is also perhaps more useful to view our algorithm as a predictor-corrector method, in which we first compute auxiliary quantities using the WENO-based portion of the algorithm, and then “correct” these quantities by removing high frequency noise from the solutions in the corrector portion of the method. Extensive testing of the method in the 1- D setting [18] shows that the noise reduction algorithm successfully eliminates high-frequency noise from the auxiliary solution, thereby producing “corrected” solutions with smaller errors. In the 2- D setting, we provide error analysis and convergence tests for the Sedov problem in Table 3. These tests indicate that the noise removal algorithm decreases the error of the computed solution; furthermore, our numerical experiments for the Noh problem in §8 and Rayleigh-Taylor problem in §12 demonstrate that, qualitatively, the noise removal algorithm greatly reduces the numerical error of solutions. Further quantitative evidence in the form of error analysis and convergence tests is presented in [19].

7 The numerical algorithm for the C -method

The systems (1), (8), (13), and (15) are discretized using a simplified finite-differencing WENO scheme for the nonlinear flux terms, and a standard central difference approximation for the diffusion terms. Time integration is done using a k^{th} order Runge-Kutta scheme. For each simulation, a fixed Δt is used at every time step, so that the CFL number can change at each time level; however, for each of the problems presented, the time step Δt is chosen so that the CFL condition is not violated at any time t during the simulation. For convenience, we provide full details of the numerical discretization of these systems in Appendix A. In particular, we refer the reader to Table 5 listing the various methods (and combinations of the methods) that we will use for the numerical tests.

We stress that the WENO-type discretization we use is highly simplified, and is not meant to be representative of the class of full WENO solvers. However, we note that, for certain problems, our simplified WENO-type discretization produces solutions with similar errors and convergence rates to those produced using a standard WENO scheme (see §5.2.5 in [18]).

As with any artificial viscosity scheme, parameters must be chosen for the particular problem under consideration. All of the relevant parameters for the schemes considered are

listed in Table 1. In [18], we suggest some practical guidelines on choosing these parameters; a brief summary of the discussion in [18] is the following. We choose the artificial viscosity parameters $\beta^{(\cdot)}$, $\beta_w^{(\cdot)}$, and η large enough to damp post-shock oscillations and high frequency noise both pre and post shock-wall collision, while the parameters ε and κ in the C -equations control the support and smoothness of the C -functions. For a more thorough discussion, we refer the reader to §5 of [18].

| Parameter / Variable | Description |
|---------------------------------------|--|
| β^u, β^E | artificial viscosity coefficients for the momentum and energy, respectively. |
| β_w^u, β_w^E | wall viscosity coefficients for the momentum and energy, respectively. |
| $\delta h, \delta_{\text{off}}, \eta$ | amplitude of noise, noise detection deactivation parameter, and noise removal viscosity, respectively. |
| $\varepsilon, \varepsilon_w$ | parameters controlling support of C (and C^{τ_i}) and C_w , respectively. |
| κ, κ_w | parameters controlling smoothness of C (and C^{τ_i}) and C_w , respectively. |

Table 1: Relevant parameters and variables used in the numerical tests.

7.1 Accuracy study: linear advection

For the purposes of demonstrating the high order convergence of the base WENO-type scheme, we consider the following linear advection equation [13, 8]

$$\partial_t \varphi(\mathbf{x}, t) + \text{div}(\mathbf{a} \varphi(\mathbf{x}, t)) = 0, \quad \mathbf{x} \in [-1, 1]^2, t > 0, \quad (22a)$$

$$\varphi(\mathbf{x}, 0) = 1 + 0.2 \sin(\pi(x + y)), \quad \mathbf{x} \in [-1, 1]^2, t = 0, \quad (22b)$$

with $\mathbf{a} = (1, -0.5)$. Periodic boundary conditions are employed, and the exact solution at time t is given by $\varphi(\mathbf{x}, t) = 1 + 0.2 \sin(\pi(x + y - 0.5t))$. The problem is run on grids with 25×25 , 50×50 , 100×100 , and 200×200 cells until the final time $t = 4$, at which time the sinusoidal wave has been advected one full wavelength. We choose the time-step so that CFL=0.8. Following [13], the relative L^1 and relative L^∞ errors are listed in percentage form in Table 2. Our simplified WENO-type scheme achieves the advertised fifth-order convergence rate, and the errors are similar to those produced with an “industry-standard” WENO method [13].

| Scheme | Error | | Cells | | | |
|--------|------------|-------|------------------------|------------------------|------------------------|------------------------|
| | | | 25×25 | 50×50 | 100×100 | 200×200 |
| WENO | L^1 | Error | 2.894×10^{-2} | 9.014×10^{-4} | 2.820×10^{-5} | 8.821×10^{-7} |
| | | Order | – | 5.005 | 4.998 | 4.999 |
| WENO | L^∞ | Error | 5.254×10^{-2} | 1.929×10^{-3} | 6.253×10^{-5} | 1.970×10^{-6} |
| | | Order | – | 4.767 | 4.947 | 4.988 |

Table 2: Relative L^1 and L^∞ errors at $t = 4$ of the computed solution minus the exact solution at and convergence for the linear advection problem. The errors are given in percentage form.

8 The Noh infinite strength shock problem

We begin our numerical experiments by considering a radially symmetric version of a classic test of Noh [15, 13]. This problem simulates an infinite strength shock wave formed by uniformly compressing a cold gas with constant velocity 1 directed towards the origin. The initial pressure is identically zero, but following [13] we use the initial value $p_0 = 10^{-6}$. The domain is $\Omega = [-1, 1]^2 \subset \mathbb{R}^2$, the adiabatic constant is $\gamma = 5/3$, and the initial data is

$$\begin{bmatrix} \rho_0 \\ (\rho u)_0 \\ (\rho v)_0 \\ E_0 \end{bmatrix} = \begin{bmatrix} 1 \\ -\cos(\theta) \\ -\sin(\theta) \\ 0.5 + 10^{-6}/(\gamma - 1) \end{bmatrix}, \quad (23)$$

where $\theta \in [0, 2\pi)$ is the polar angle. The final time is $t = 2.0$.

The exact solution consists of a shock front moving radially outwards into the cold gas with speed $1/3$. The shock is of “infinite strength”, since the sound speed satisfies $c = 0$ in the cold gas. The numerical solution is computed in the positive quadrant $[0, 1]^2$ and then reflected appropriately to yield the solution on all of $[-1, 1]^2$. Consequently, reflecting boundary conditions are employed on the x and y axes. The exact solution is used to enforce the boundary conditions at the boundaries $x = 1$ and $y = 1$ (see [13] for the details).

The Noh test is a difficult problem; among the numerical methods considered in [13], only the PPM and CFLFh schemes produce somewhat satisfactory solutions with sharp shock fronts, though the solutions are still noisy and have large errors at the origin due to the phenomenon of anomalous *wall-heating* [21, 18, 13, 15]. In particular, the WENO scheme considered in [13] fails for this problem. Consequently, it is not so surprising that our grossly simplified WENO scheme also fails for this problem. That is to say, our stand-alone WENO scheme is unable to run until the final time $t = 2.0$; the solution develops noise in the region with the cold gas, which eventually causes a violation of the positivity of the density and, subsequently, blow-up of the solution. This is the case even for a very small time-step δt ; using $\text{CFL} = 5.0 \times 10^{-3}$ still results in blow-up. We propose the use of the C -method and the noise detection and removal algorithm to deal with these issues.

8.1 Application of WENO- C - N to the Noh problem

We will apply the WENO- C - N scheme on a grid with 200×200 cells in the domain $[0, 1]^2$ with a time-step $\delta t = 5 \times 10^{-4}$, giving a CFL number of approximately 0.25. A modified

noise detection algorithm is employed, which we now describe. The “input functions” in the noise detection procedure described in §6.3 are the (potentially noisy) horizontal and vertical velocities $\tilde{u}(x, y)$ and $\tilde{v}(x, y)$. The noise detection procedure for each of these functions produces two different “noise indicator functions”, denoted by $\mathbb{1}_{\text{noise}}^u(x, y)$ and $\mathbb{1}_{\text{noise}}^v(x, y)$. The function $\mathbb{1}_{\text{noise}}^u(x, y)$ is then used to de-noise the velocity field \tilde{u} , while $\mathbb{1}_{\text{noise}}^v(x, y)$ is used to de-noise \tilde{v} . For the Noh problem, we exploit the radial symmetry available by using the radial velocity $\tilde{u}_r(x, y) := \cos(\theta)\tilde{u}(x, y) + \sin(\theta)\tilde{v}(x, y)$ to produce a noise indicator function $\mathbb{1}_{\text{noise}}^r(x, y)$, where θ is the polar angle. The de-noising procedure for \tilde{u} and \tilde{v} then uses the function $\mathbb{1}_{\text{noise}}^r(x, y)$, but is otherwise identical to the algorithm described in §6.2 and §6.3.

The parameters for the WENO- C - N scheme are chosen as

$$\begin{aligned} \beta^u &= 50.0, & \beta^E &= 350.0, & \varepsilon &= 200.0, & \kappa &= 0.5, \\ \eta \cdot \delta\tau / |\delta\mathbf{x}|^2 &= 5 \times 10^{-2}, & \delta h &= 10^{-5}, & \delta_{\text{off}} &= 0.2. \end{aligned}$$

The artificial viscosity term on the right-hand side of the energy equation (8d) serves to correct for the wall-heating error. The local heat equation solver for noise removal is iterated for a single time step only.

We provide in Fig.10 a heatmap plot of the density computed using WENO- C - N , as well as a scatter plot of the density versus radius. We see that the space-time smooth artificial diffusion provided by the C -method stabilizes the strong shock wave and prevents spurious oscillations from developing behind the solution, while the artificial heat conduction term on the right-hand side of the energy equation (8d) significantly reduces the wall-heating error. The noise detection and removal procedure prevents high frequency noise from corrupting the solution and does not affect the sharpness of the shock front. Moreover, the solution maintains, for the most part, angular symmetry, though there are minor variations in the azimuthal direction; this should be contrasted with the results presented in [13], which show a much more obvious lack of symmetry by other schemes.

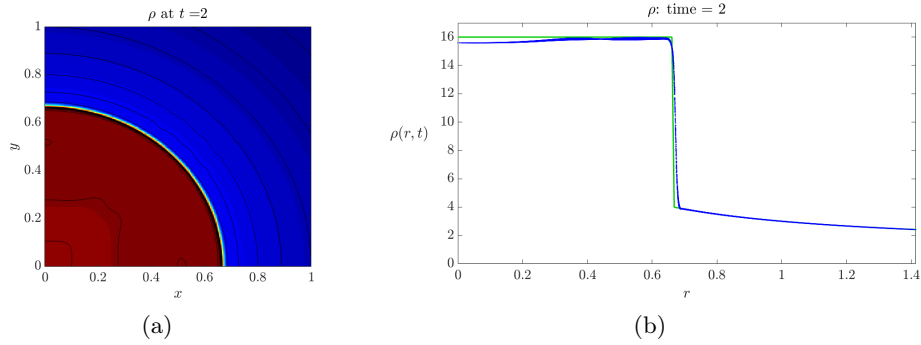


Figure 10: Application of WENO- C - N to the Noh problem on the grid $[0, 1]^2$ with 200×200 cells. Shown on the left is a heatmap of the density ρ at time $t = 2.0$. This is overlaid by 23 density contours, from 2.5 to 4 with step 0.25, and 14 to 17 with step 0.2. On the right is a scatter plot of the density versus radius. The green curve is the exact solution.

8.2 Comparison with Noh's artificial viscosity scheme

For the purposes of comparison, we also implement our WENO scheme together with a modification of Noh's artificial viscosity scheme [15], which is designed specifically for the Noh problem. The resulting scheme is referred to as WENO-Noh. Noh's scheme couples the classical artificial viscosity method of Von Neumann and Richtmeyer with a heat conduction term for the energy equation. In particular, the diffusion terms on the right-hand sides of (8b), (8c), and (8d) are replaced with the terms

$$\operatorname{div} \left(\tilde{\beta}_N^u \rho |\nabla u_r| \nabla u \right) + \tilde{\alpha}_N^u \Delta u, \quad (24a)$$

$$\operatorname{div} \left(\tilde{\beta}_N^u \rho |\nabla u_r| \nabla v \right) + \tilde{\alpha}_N^u \Delta v, \quad (24b)$$

$$\operatorname{div} \left(\tilde{\beta}_N^e \rho |\nabla u_r| \nabla e \right) + \tilde{\alpha}_N^e \Delta e, \quad (24c)$$

respectively, where u_r is the radial velocity, $e = p/\rho(\gamma - 1)$ is the internal energy of the system, and the artificial viscosity parameters $\tilde{\beta}_N$ and $\tilde{\alpha}_N$ are defined by

$$\tilde{\beta}_N = \frac{|\delta \mathbf{x}|^2}{\max_{\Omega} |\nabla u_r|} \beta_N \quad \text{and} \quad \tilde{\alpha}_N = |\delta \mathbf{x}| \alpha_N.$$

The parameter β_N controls the amount of *classical artificial viscosity* added to the system, while the parameter α_N controls the amount of *linear viscosity* added to the system. We refer the reader to [18] for a discussion on the differences between the diffusion terms used in WENO-Noh and the diffusion terms used in WENO- C - N .

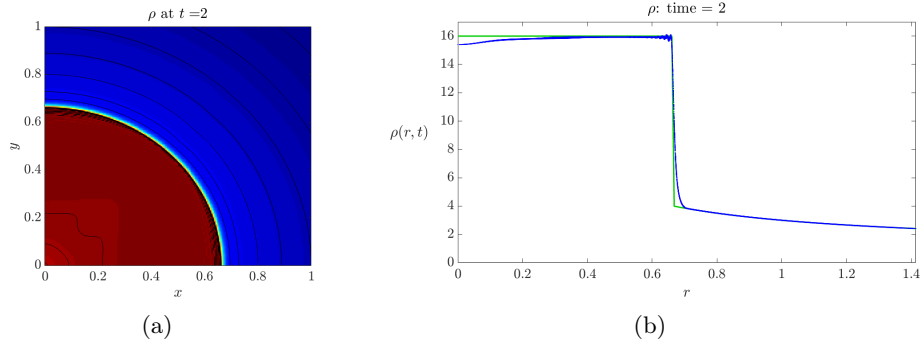


Figure 11: Application of WENO-Noh to the Noh problem on the grid $[0, 1]^2$ with 200×200 cells. Shown on the left is a heatmap of the density ρ at time $t = 2.0$. This is overlaid by 23 density contours, from 2.5 to 4 with step 0.25, and 14 to 17 with step 0.2. On the right is a scatter plot of the density versus radius. The green curve is the exact solution.

We implement the above WENO-Noh scheme for the Noh problem, with the following choices of viscosity parameters: $\beta_N^u = 50.0$, $\beta_N^e = 350.0$, $\alpha_N^u = 0.5$, and $\alpha_N^e = 1.5$. The results are shown in Fig.11. The WENO-Noh scheme produces a solution that is, for the most part, oscillation-free; however, there are still some oscillations in the density profile behind the shock, and the shock curve is overly smeared. We remark here that the use of

the linear viscosity term in (24) was needed to allow the WENO-Noh scheme to run; indeed, when that linear viscosity term was removed, the numerical simulation could not run as the solution blew-up. This is due primarily to the extremely oscillatory nature of the localizing function $|\nabla u_r|$; the additional linear viscosity stabilized the solution, at the cost of a very smeared shock curve and a loss of accuracy.

The solution produced with WENO- C - N has a much sharper shock front. In fact, a simple computation shows that $\max_{\Omega} |\nabla \rho(x, y, 2)| \approx 856$ and $\max_{\Omega} |\nabla \tilde{\rho}(x, y, 2)| \approx 774$, where ρ is the WENO- C - N solution for the density and $\tilde{\rho}$ is the WENO-Noh solution for the density. Consequently, we see that WENO- C - N produces a less oscillatory, more accurate solution with a sharper shock front.

9 The Sedov blast wave

The Sedov problem [22, 31, 1] models the self-similar evolution of a cylindrical blast wave, arising from a point-source explosion in a cold, uniform density fluid. The computational domain is $\Omega = [0, 1.2] \times [0, 1.2] \subset \mathbb{R}^2$. The initial density and velocity are, respectively, $\rho_0 = 1$, $u_0 = v_0 = 0$, and the initial energy is set to $E_0 = 10^{-12}$ everywhere except in the lower left corner cell, where it takes the value $\frac{0.244816}{\delta x \cdot \delta y}$. The adiabatic constant is $\gamma = 1.4$, reflecting boundary conditions are employed at the bottom and left boundaries, while inhomogeneous Dirichlet boundary conditions are enforced on the top boundary and the right boundary; in particular, the velocity, density, and energy are set equal to the corresponding values of the initial data on those boundaries.

The solution consists of an infinite strength radially symmetric shock front propagating outwards from the origin, leaving behind a near vacuum state. The simulation is run until time $t = 1.0$, at which time the shock front is a circle with radius equal to 1. A semi-exact solution exists for this problem [23, 10, 11], and we shall use the code made available by [33] to compute this solution. Our WENO and WENO- C - N schemes are employed on a grid with 96 cells in both directions, and with a time-step $\delta t = 10^{-4}$. This fixed time-step was chosen as the largest possible value for which the WENO simulation runs on the desired time interval. For the noise detection portion of our WENO- C - N scheme, we utilize the modified algorithm for radially symmetric flow, described in §8.1 for the Noh problem. The parameters for the C - N -method are as follows:

$$\begin{aligned} \beta^u &= 1.0, & \beta^E &= 10.0, & \varepsilon &= 1.0, & \kappa &= 0.5, \\ \eta \cdot \delta \tau / |\delta \mathbf{x}|^2 &= 10^{-2}, & \delta h &= 10^{-4}, & \delta_{\text{off}} &= 0.02. \end{aligned}$$

The results are shown in Figs.12 and 13. Our stand-alone WENO scheme produces a solution with inaccurate shock speed and location, and is corrupted by a large amount of high-frequency oscillations (or noise) behind the shock front. On the other hand, our WENO- C - N algorithm provides a solution with accurate wave speed and location, stabilizes the dynamics during early time-steps, and removes high-frequency oscillations behind the shock front.

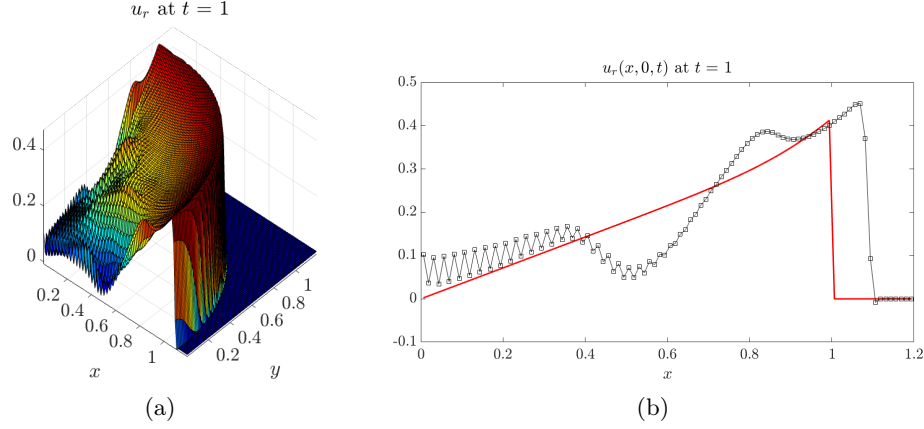


Figure 12: Application of our standalone WENO scheme to the Sedov problem on the grid $[0, 1.2]^2$ with 96×96 cells. Shown are (a) a surface plot of the radial velocity u_r , (b) u_r along the cut $y = 0$. The red curves are the exact solutions.

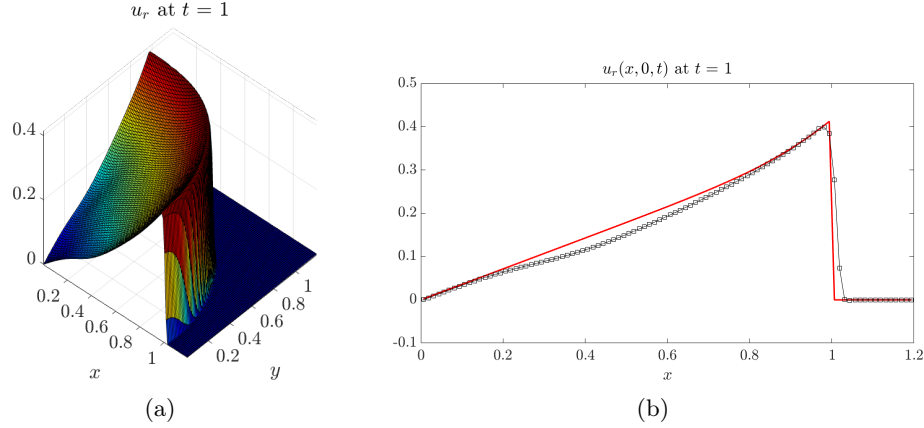


Figure 13: Application of WENO- $C-N$ to the Sedov problem on the grid $[0, 1.2]^2$ with 96×96 cells. Shown are (a) a surface plot of the radial velocity u_r , (b) u_r along the cut $y = 0$. The red curves are the exact solutions.

We next conduct L^1 error analysis and convergence tests for the Sedov problem. Due to the fact that the exact solution is known only in radial coordinates, and our solution is defined on a rectangular mesh, we shall compute the errors of the density ρ and radial velocity u_r along the cut $y = 0$. We thus define the quantities $\tilde{\rho} = \rho(x, 0, t) - \rho^*(x, t)$ and $\tilde{u}_r = u_r(x, 0, t) - u_r^*(x, t)$, where ρ^* and u_r^* are the exact solutions. The L^1 norm for a function $f(x)$ defined on a one-dimensional computational grid of M cells with cell centers x_i is defined as

$$\|f\|_{L^1} = \frac{1}{M} \sum_{i=1}^M |f(x_i)|. \quad (25)$$

In Table 3, we list the L^1 norms and order of convergence for the errors $\tilde{\rho}$ and \tilde{u}_r . For the

solution produced with the stand-alone WENO algorithm, the presence of the computational noise and the incorrect shock speed result in large errors and poor convergence rates⁴. The shock stabilization and noise removal provided by the WENO- C - N algorithm produces solutions with much smaller errors than those computed with stand-alone WENO, as well as better rates of convergence.

| Norm | Scheme | | Cells | | |
|--------------------------|-----------------|-------|------------------------|------------------------|------------------------|
| | | | 24 | 48 | 96 |
| $\ \tilde{\rho}\ _{L^1}$ | WENO | Error | 6.347×10^{-1} | 4.722×10^{-1} | 4.648×10^{-1} |
| | | Order | – | 0.427 | 0.023 |
| | WENO- C - N | Error | 3.939×10^{-1} | 1.081×10^{-1} | 5.765×10^{-2} |
| | | Order | – | 1.866 | 0.907 |
| $\ \tilde{u}_r\ _{L^1}$ | WENO | Error | 2.113×10^{-1} | 8.993×10^{-2} | 7.266×10^{-2} |
| | | Order | – | 1.232 | 0.308 |
| | WENO- C - N | Error | 4.695×10^{-2} | 1.979×10^{-2} | 1.482×10^{-2} |
| | | Order | – | 1.247 | 0.417 |

Table 3: L^1 error analysis and convergence tests for the Sedov problem at $t = 1.0$.

In Fig.14, we show plots of the computed density ρ and radial velocity u_r along the cut $y = 0$ at various grid resolutions. It is clear from these plots, as well as the data in Table 3, that WENO- C - N produces solutions that are both quantitatively and qualitatively better than those produced with WENO.

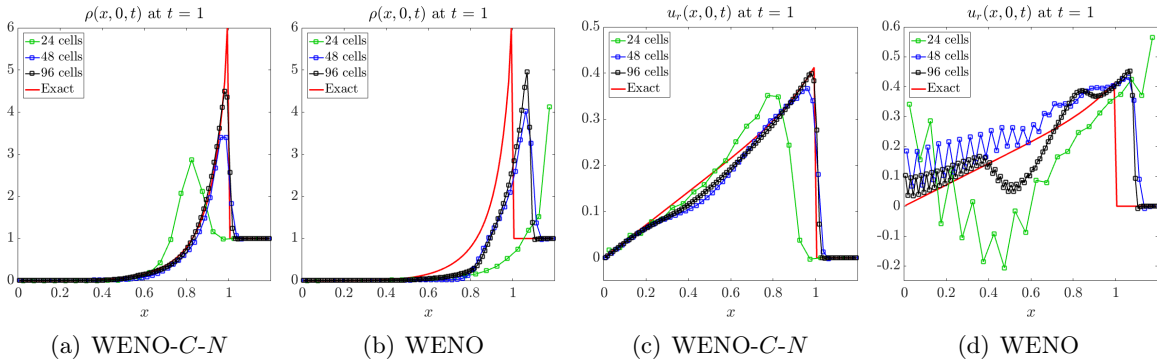


Figure 14: Plots of (a,b) the density and (c,d) the radial velocity along the cut $y = 0$. Subfigures (a) and (c) show the solutions computed with WENO- C - N , while Subfigures (b) and (d) show the solutions computed with WENO.

⁴We note the “super-convergence” [8] of the WENO solutions on the coarse grids; this is due to large errors on coarser meshes, rather than smaller errors on finer meshes, and is therefore superficial.

10 The Sod circular explosion problem

The explosion problem proposed in [34, 13] is a radially symmetric version of the classic Sod shock tube problem [28].

$$\begin{bmatrix} \rho_0 \\ (\rho u)_0 \\ (\rho v)_0 \\ E_0 \end{bmatrix} = \begin{bmatrix} 1 \\ 0 \\ 0 \\ 2.5 \end{bmatrix} \mathbb{1}_{[0,0.4)}(r) + \begin{bmatrix} 0.125 \\ 0 \\ 0 \\ 0.25 \end{bmatrix} \mathbb{1}_{[0.4,\infty)}(r), \quad (26)$$

where $r = \sqrt{x^2 + y^2}$, and $\mathbb{1}_\Sigma$ denotes the indicator function on the set Σ . We remark that the initial conditions are implemented in [13, 34] by assigning area-weighted initial values for the cells which are crossed by the initial curve of discontinuity. We omit this modification, noting that an instability develops at the contact surface regardless of whether the area-weighted initial conditions are implemented. Since we wish to capture the evolution of the unstable contact, we do not smear the initial data, and instead employ our anisotropic artificial viscosity method.

Reflecting boundary conditions are employed on the x and y axes, and free-flow boundary conditions are employed at the boundaries $x = 1.5$ and $y = 1.5$. The free-flow boundary conditions are implemented using the characteristic form of the Euler equations so as to minimize the reflection from the outgoing waves (see [32] for the details). Nonetheless, there are numerical boundary effects occurring at the top and right boundaries that we were unable to eliminate.

The solution consists of a circular shock front and contact curve traveling outwards from the origin, and a circular expansion wave traveling inwards to the origin. The shock front and contact surface become weaker as time evolves, with the contact eventually coming to rest before traveling inwards, while the shock front passes through the free-flow boundary. The rarefaction wave traveling inwards collides with itself at the origin and reflects as an outwards traveling expansion wave. This results in an inward traveling shock forming and subsequently imploding into the origin. This shock then reflects outwards from the origin and eventually passes through the contact curve.

We shall demonstrate the ability of the C -method to allow the artificial viscosity operator associated with the shock wave to “communicate” with the artificial viscosity operator associated to the contact discontinuity. The objective of the scheme is to allow the shock wave to pass through the contact discontinuity, while leaving the small-scale KH structure of the contact undisturbed by over-diffusion. Our results compare favorably to those produced by PPM, CLAW, and WAFT [13].

10.1 The WENO- $C-\hat{C}$ scheme applied to the Sod explosion problem

We employ a combination of our WENO- C and WENO- C^τ schemes for this problem. More precisely, we use isotropic artificial viscosity (as provided by the WENO- C scheme) to stabilize shock fronts, and anisotropic tangential artificial viscosity (as provided by the WENO- C^τ scheme) to add diffusion to the unstable contact curve. We utilize a combination of compression and expansion switches to track the contact curve and shock fronts. In

particular, we remark that, since shock implosion is a highly singular phenomenon, the shock that reflects from the origin requires stabilization. However, this shock passes through the contact curve, and consequently we ensure that the stabilization of the shock does not result in an overly diffused contact discontinuity. We do so by turning-off the artificial viscosity on the shock front as it passes through the contact curve by using compression and expansion switches (which are detailed below).

More precisely, we consider the following Euler- C - \hat{C} system:

$$\partial_t \rho + \operatorname{div}(\rho \mathbf{u}) = 0, \quad (27a)$$

$$\partial_t(\rho u) + \partial_x(\rho u^2 + p) + \partial_y(\rho uv) = \operatorname{div} \left(\tilde{\beta}^u \rho C \nabla u \right) + \partial_i \left(\tilde{\alpha} \rho \hat{C} C^{\tau_i} C^{\tau_j} \partial_j u \right), \quad (27b)$$

$$\partial_t(\rho v) + \partial_x(\rho uv) + \partial_y(\rho v^2 + p) = \operatorname{div} \left(\tilde{\beta}^v \rho C \nabla v \right) + \partial_i \left(\tilde{\alpha} \rho \hat{C} C^{\tau_i} C^{\tau_j} \partial_j v \right), \quad (27c)$$

$$\partial_t E + \operatorname{div}(\mathbf{u}(E + p)) = \operatorname{div} \left(\tilde{\beta}^E \rho C \nabla (E/\rho) \right), \quad (27d)$$

$$\partial_t C - \mathcal{L}[C; \varepsilon, \kappa] = \frac{S(\mathbf{u})}{\varepsilon |\delta \mathbf{x}|} G_\rho \quad (27e)$$

$$\partial_t \hat{C} - \mathcal{L}[\hat{C}; \varepsilon, \kappa] = \frac{S(\mathbf{u})}{\varepsilon |\delta \mathbf{x}|} \hat{G}_\rho, \quad \partial_t C^{\tau_i} - \mathcal{L}[C^{\tau_i}; \varepsilon, \kappa] = \frac{S(\mathbf{u})}{\varepsilon |\delta \mathbf{x}|} \hat{\tau}_i \text{ for } i = 1, 2. \quad (27f)$$

The forcing functions to the C -equations are given by

$$G_\rho = [1 - \mathbb{1}_{(-\infty, 0)}(\partial_r e \partial_r \rho)] \cdot \mathbb{1}_{(-\infty, 0)}(\operatorname{div} \mathbf{u}) \cdot |\nabla \rho|, \quad (28a)$$

$$\hat{G}_\rho = \mathbb{1}_{(-\infty, 0)}(\partial_r e \partial_r \rho) \cdot |\nabla \rho|, \quad (28b)$$

$$\hat{\tau}_1 = -\mathbb{1}_{(-\infty, 0)}(\partial_r e \partial_r \rho) \cdot \partial_y \rho, \quad (28c)$$

$$\hat{\tau}_2 = \mathbb{1}_{(-\infty, 0)}(\partial_r e \partial_r \rho) \cdot \partial_x \rho, \quad (28d)$$

where $\partial_r = \cos \theta \partial_x + \sin \theta \partial_y$ denotes the radial derivative. The function $\mathbb{1}_{(-\infty, 0)}(\operatorname{div} \mathbf{u})$ is a compression switch that localizes C to shocks, while the function $\mathbb{1}_{(-\infty, 0)}(\partial_r e \partial_r \rho)$ localizes \hat{C} and $\hat{\tau}_i$ to the contact curve. Consequently, the use of the function $[1 - \mathbb{1}_{(-\infty, 0)}(\partial_r e \partial_r \rho)]$ in (28a) ensures that C deactivates during the short time interval that the shock front passes through the contact, so that isotropic diffusion is not added during this time interval, which prevents the smearing of the contact curve.

The artificial viscosity parameters $\tilde{\beta}$ and $\tilde{\alpha}$ are defined by

$$\tilde{\beta}^\cdot = \frac{|\delta \mathbf{x}|^2}{\max_\Omega C} \beta^\cdot \quad \text{and} \quad \tilde{\alpha} = \frac{|\delta \mathbf{x}|^2}{\mu^2 \max_\Omega \hat{C}} \alpha,$$

with $\mu = \max_\Omega \{\max\{|C^{\tau_1}|, |C^{\tau_2}|\}\}$.

The Euler- C - \hat{C} system is numerically discretized in an identical fashion to the other schemes presented; we will refer to the discretized method as the WENO- C - \hat{C} scheme. We employ the method to the problem on a grid with 400×400 cells with a time-step of

$\delta t = 6.4 \times 10^{-4}$, giving an initial CFL number of approximately 0.75. The parameters for the WENO- $C-\hat{C}$ method are chosen as

$$\beta^u = 15.0, \quad \beta^E = 200.0, \quad \alpha = 2.0, \quad \varepsilon = 1.0, \quad \kappa = 10.0.$$

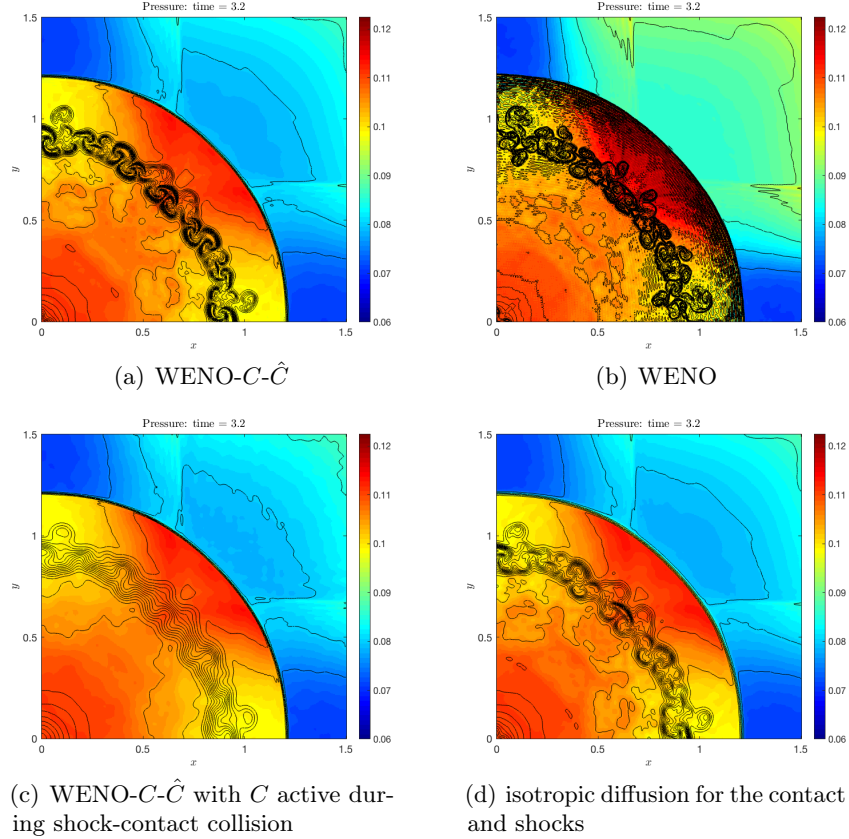


Figure 15: Comparison of WENO and WENO- $C-\hat{C}$ for the Sod explosion problem. The figures shown are heatmap plots of the pressure p overlaid with 27 density contours from 0.08 to 0.21 with step 0.005. Results are presented at time $t = 3.2$.

The results are presented in Fig.15, which show heatmap plots of the pressure function p overlaid with density contours. These figures should be contrasted with those presented in [13]. The stand-alone WENO scheme produces a highly oscillatory solution behind the shock front (see Fig.15(b)), whereas the C -method allows for the stabilization of the shock front. Additionally, we may see the role that the function $[1 - \mathbb{1}_{(-\infty, 0)}(\partial_r e \partial_r \rho)]$ plays by comparing with the solution computed without the deactivation of C during shock-contact collision; this solution, shown in Fig.15(c), is noticeably more smeared at the contact discontinuity. Finally, in Fig.15(d) we show the solution computed using isotropic diffusion for both the contact discontinuity as well as shock fronts, with all the relevant parameters identical to those used in the WENO- $C-\hat{C}$ simulation. It is clear that the contact discontinuity is not as sharp as the contact curve for the solution computed using WENO- $C-\hat{C}$; this is due to the addition of

diffusion in the direction normal to the contact curve. The WENO- $C-\hat{C}$ scheme produces a non-oscillatory solution with minimal noise, a sharp shock front, and a sharp contact curve.

10.2 Shock-wall collision for a Sod-type explosion problem

To test the shock-collision scheme presented in §5, we consider a modified version of the Sod circular explosion problem. The domain is $\Omega = [-1, 1] \times [-0.7, 1.3] \subset \mathbb{R}^2$, the adiabatic constant is $\gamma = 1.4$, and the initial data is

$$\begin{bmatrix} \rho_0 \\ (\rho u)_0 \\ (\rho v)_0 \\ E_0 \end{bmatrix} = \begin{bmatrix} 1 \\ 0 \\ 0 \\ 2.5 \end{bmatrix} \mathbb{1}_{[0,0.1)}(r) + \begin{bmatrix} 0.125 \\ 0 \\ 0 \\ 0.25 \end{bmatrix} \mathbb{1}_{[0.1,\infty)}(r), \quad (29)$$

where $r = \sqrt{x^2 + y^2}$, and $\mathbb{1}_\Sigma$ denotes the indicator function on the set Σ .

We are interested in the problem of shock-wall collision, and so treat the bottom boundary as a fixed wall, so that solid-wall (or reflecting) boundary conditions are enforced at $y = -0.7$. Free-flow (or symmetric) boundary conditions are implemented at the other three boundaries. The final time is $t = 0.6$. The outwards traveling shock front collides with the bottom boundary $y = -0.7$ at time $t \approx 0.4$. As the gas is compressed, an increase in the density leads to a reversal in the direction of travel of the shock front. The collision with the bottom boundary breaks the radial symmetry of the problem; since the first point of contact of the shock front with the bottom boundary occurs at $x = 0$, the gas is forced outwards along the bottom boundary $y = -0.7$.

We employ our WENO- $C-W$ scheme (see §5), which couples the C -method with a shock collision scheme. Due to the symmetry of the problem, we compute the solution in the half domain $[0, 1] \times [-0.7, 1.3]$, and then reflect appropriately to obtain the solution on all of Ω . The WENO- $C-W$ scheme is applied on a grid with 200×400 cells in the half domain $[0, 1] \times [-0.7, 1.3]$, with a time-step $\delta t = 5 \times 10^{-4}$, giving a CFL number of approximately 0.4. The parameters in the WENO- $C-W$ method are chosen as

$$\begin{aligned} \beta^u &= 20.0, & \beta^E &= 0.0, & \varepsilon &= 1.0, & \kappa &= 1.0, \\ \beta_w^u &= 50.0, & \beta_w^E &= 100.0, & \varepsilon_w &= 10.0, & \kappa_w &= 1.0. \end{aligned}$$

For the purposes of comparison, we also implement our stand-alone WENO scheme as well as the WENO-Noh scheme with the following modification: due to the loss of radial symmetry when the shock front collides with the bottom boundary $y = 0$, we do not use the (normalized) gradient of the radial velocity $|\nabla u_r| / \max_\Omega |\nabla u_r|$ to track the shock front; instead, we use the function $\mathbb{1}_{\text{div} \mathbf{u} < 0} |\nabla \rho| / \max_\Omega |\nabla \rho|$, where $\mathbb{1}_{\text{div} \mathbf{u} < 0}$ is a compression switch. The artificial viscosity parameters in (24) are chosen as

$$\alpha_N^u = \alpha_N^e = 0 \quad \text{and} \quad \beta_N^u = 70.0, \beta_N^e = 200.0.$$

The results are provided in Fig.16, which shows surface plots of the density, and Fig.17, which is a plot of the vertical velocity $v(0, y, t)$ along $x = 0$.

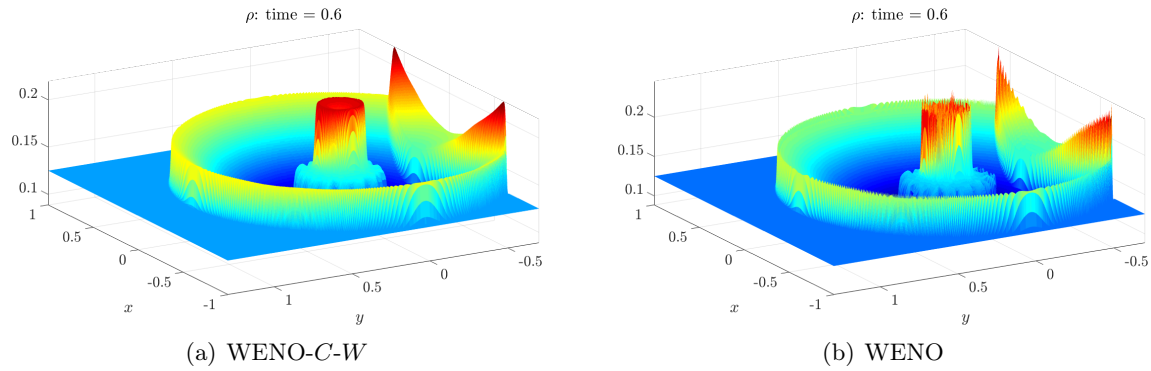


Figure 16: Comparison of WENO and WENO- C - W for the Sod explosion and bounce-back problem. The figures shown are surface plots of the density ρ after shock-wall collision.

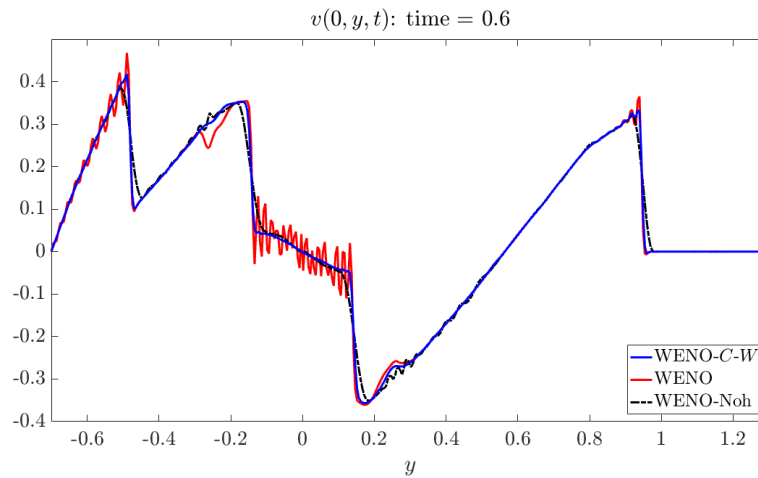


Figure 17: Comparison of WENO, WENO-Noh, and WENO- C - W for the Sod explosion and bounce-back problem. Shown are cross-sections of the vertical velocity $v(0, y, t)$ along $x = 0$, at time $t = 0.6$ after the shock-wall collision.

The stand-alone WENO scheme produces an oscillatory solution both pre and post shock-wall collision. In particular, the shock implosion at the origin results in a large amount of noise (see Fig.17). The solution computed using WENO-Noh is also oscillatory, albeit to a lesser extent, and the shock fronts are overly smeared. On the other hand, the WENO- C - W scheme produces a solution that is completely noise-free while retaining sharp shock fronts and correct wave speeds.

11 The Mach 10 shock reflection problem

The double Mach shock reflection problem introduced by Woodward & Colella [5] features a Mach 10 shock in a $\gamma = 1.4$ gas reflecting from a wedge inclined at an angle of 60° . The

computational domain is $\Omega = [0, 3.25] \times [0, 1]$, and the initial data is given by

$$\begin{bmatrix} \rho_0 \\ (\rho u)_0 \\ (\rho v)_0 \\ E_0 \end{bmatrix} = \begin{bmatrix} 8 \\ 66 \cos(\pi/6) \\ -66 \sin(\pi/6) \\ 563.5 \end{bmatrix} \mathbb{1}_{\Sigma}(x, y) + \begin{bmatrix} 1.4 \\ 0 \\ 0 \\ 1.0 \end{bmatrix} \mathbb{1}_{\Omega \setminus \Sigma}(x, y), \quad (30)$$

where $\Sigma = \{(x, y) \in \Omega \mid y > \sqrt{3}(x - 1/6)\}$ is the region behind the initial position of the shock. On the left boundary, the density, velocity, and energy are prescribed the values of the corresponding initial conditions, while free-flow boundary conditions are imposed at the right boundary. The conditions at the top boundary are set to describe the exact motion of the initial Mach 10 shock. At time t , the shock intersects with the top boundary $y = 1$ at the point $(s(t), 1)$, where $s(t) = 1/6 + (1 + 20t)/\sqrt{3}$. The pre- and post-shock conditions are then imposed for $x \geq s(t)$ and $x < s(t)$, respectively. At the bottom boundary, reflecting boundary conditions are prescribed, except for the short region $0 \leq x < 1/6$, along which the exact initial conditions are imposed. This condition forces the reflected shock to remain “attached” to the wedge.

The solution develops a complex self-similar flow structure featuring two triple points and a jet attached to bottom wall. Numerical methods applied to this problem often produce solutions suffering from the “carbuncle phenomenon” [16]. In such solutions, the wave speed of the leading Mach stem is incorrect, leading to a “kink” in the stem, and often the formation of a spurious additional triple point. In fact, our simplified WENO-type scheme produces a solution, shown in Fig.18, exhibiting this error; moreover, the solution is corrupted by a large amount of high frequency noise, especially in the regions where the shock fronts meet with the reflecting wall.

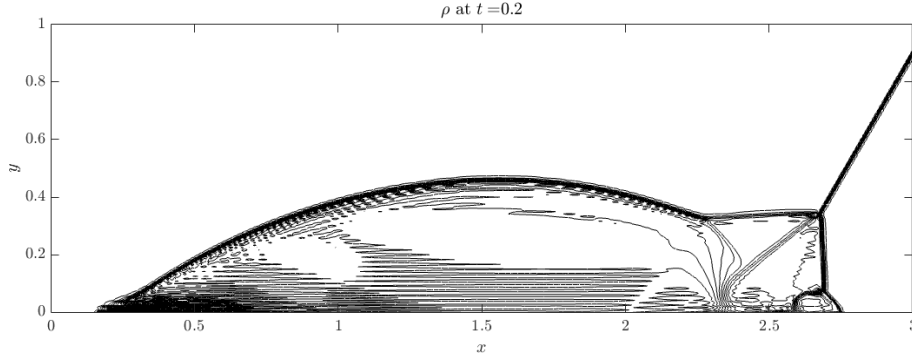


Figure 18: A density contour plot of the stand-alone WENO solution computed on a grid with $\delta x = \delta y = 1/120$. Shown are 30 equally spaced density contours from $\rho = 1.5$ to $\rho = 22.9705$. The carbuncle instability leads to a kink at the leading shock front, causing a spurious triple point to form. There are high-frequency oscillations behind the reflected shock front, especially in the regions where shock curves intersect with the reflecting wall.

To eliminate the carbuncle error and the high-frequency noise in the computed solution near the reflecting wall, we shall employ our WENO- C - W algorithm for this problem, with the following simple modification: since there is noise in the solution near the wall-jet, we do

not use the compression switch $\mathbb{1}_{\text{div}\mathbf{u}<0}$ in the C -equation (15e). This allows the C -function to remain active at the wall-jet, so that the artificial viscosity damps the high-frequency oscillations in this region. The discontinuities are stabilized through the use of directionally isotropic viscosity, and the wall C -method is used to implement additional viscosity in the regions where the shock fronts meet with the bottom reflecting boundary. We note that the compression switch $\mathbb{1}_{\text{div}\mathbf{u}<0}$ remains active for the wall C equation (15f); this forces the wall function $\overline{C}(x, t)$ to vanish at the wall-jet, which subsequently prevents the over-smearing of the contact discontinuity.

We implement the WENO- C - W scheme, with the small modification mentioned above, on a grid with 781×241 cells, giving a mesh resolution of $\delta x = \delta y = 1/240$. The time-step is set as $\delta t = 4 \times 10^{-5}$, giving $\text{CFL} \approx 0.4$. This time-step was chosen as the largest possible value for which the stand-alone WENO simulation runs until the final time $t = 0.2$. The relevant parameters for the WENO- C - W method are chosen as

$$\begin{aligned} \beta^u &= 3 \times 10^2, & \beta^E &= 0.0, & \varepsilon &= 10.0, & \kappa &= 1.0, \\ \beta_w^u &= 1 \times 10^3, & \beta_w^E &= 0, & \varepsilon_w &= 10.0, & \kappa_w &= 1.0. \end{aligned}$$

A contour plot of the density computed using WENO- C - W is shown in Fig.19. The artificial viscosity stabilizes the shock fronts and corrects the wave speeds, resulting in the elimination of the spurious carbuncle instability at the leading shock. Moreover, the high-frequency oscillations at the intersections of shock fronts with the bottom boundary, and near the wall-jet, are suppressed by the additional viscosity provided by the wall C -method active in those regions. Our result is comparable to the simulations presented, for example, by Shi, Zhang, & Shu [25], for their developed WENO schemes.

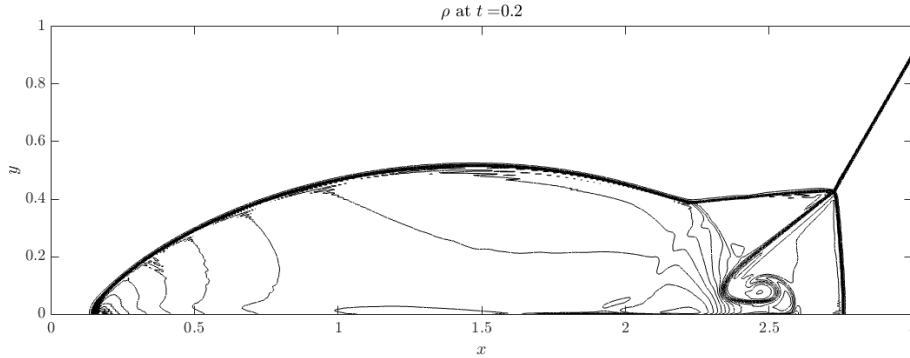


Figure 19: A density contour plot of the WENO- C - W solution computed on a grid with $\delta x = \delta y = 1/240$. Shown are 30 equally spaced density contours from $\rho = 1.5$ to $\rho = 22.9705$.

12 The Rayleigh-Taylor instability

The Rayleigh-Taylor (RT) instability [17, 30] is an instability of a heavy fluid layer supported by a light one. Specifically, RT occurs when a perturbed interface, between two fluids of different density, is subjected to a normal pressure gradient; the light fluid *bubbles* into the heavy fluid, while the heavy fluid *spikes* into the lighter fluid, which in turn initiates the

Kelvin-Helmholtz (KH) instability. The RT instability occurs in a wide range of physical phenomena; see [24, 12] and the references therein for an overview.

We use the following setup for the RT problem considered by Liska & Wendroff [13]: the domain is $\Omega = [-1/6, +1/6] \times [0, 1]$, the adiabatic constant is $\gamma = 1.4$, and the initial data is

$$\begin{bmatrix} \rho_0 \\ (\rho u)_0 \\ (\rho v)_0 \\ E_0 \end{bmatrix} = \begin{bmatrix} 1 \\ 0 \\ 0 \\ p_0/(\gamma - 1) \end{bmatrix} \mathbb{1}_{[0, h_0)}(y) + \begin{bmatrix} 2 \\ 0 \\ 0 \\ p_0/(\gamma - 1) \end{bmatrix} \mathbb{1}_{[h_0, 1]}(y). \quad (31)$$

Here, the initial interface Γ_0 is parameterized by $(x, h_0(x))$ with $h_0(x) = 0.5 + 0.01 \cos(6\pi x)$, and p_0 is the initial pressure, defined as

$$p_0 = \begin{cases} P_0 + g(h_0(x) - y) + 2g(1 - h_0(x)) & , \text{ if } y < h_0(x) \\ P_0 + 2g(1 - y) & , \text{ if } y \geq h_0(x) \end{cases}, \quad (32)$$

with $g = 0.1$ the gravitational acceleration, and P_0 the reference pressure. While Liska & Wendroff [13] do not provide P_0 , we follow the ATHENA code [29] and use the value $P_0 = 2.4$ so as to produce a sound speed $c = \sqrt{3.5}$ in the lower density gas at the interface. The equations of motion governing the flow are given by the Euler system (1) with the addition of the gravity forcing on the right-hand side of (1a): $\mathbf{f} = [0, 0, -g\rho, -g\rho v]^T$. Due to the symmetry of the problem, it is sufficient to calculate the solution in the half-domain $[0, 1/6] \times [0, 1]$, and then use reflection.

For a very short time, when the amplitude of the perturbation remains very small compared with the wavelength of the perturbation, the motion of the interface can be analyzed using linear stability analysis [17, 30, 3, 14]. Quickly, however, the nonlinearity is activated, and the interface evolves to the classical “mushroom-shaped” profile [35]. The flow at later times is characterized by the development of “roll-up” regions, driven by the KH shear instability [12].

The particular problem set up described above results in a low Mach number flow. For explicit time-integration schemes, the CFL stability condition requires the time-step to be very small for such flows, due to the fact that, in this regime, sound waves are much faster than the advection of the flow. We do not switch to implicit time-integration, but note that one of the authors has extensively compared implicit and explicit temporal differencing for low Mach number flows and found little differences between the two approaches, provided the time step size is below the sound speed in the explicit approach; the time step size can be at least a factor of 10 bigger in the implicit approach. Likewise, for time-split methods, it has been shown that time-split errors grow as the time step begins to exceed the fastest time scale of the problem, i.e. the speed of sound waves. Hence, it is presumed for the current algorithm, in which the time steps utilized are below this fast time scale, that the temporal error growth is small. Moreover, we note that explicit time integration is used by Liska & Wendroff [13], and so for the purposes of comparison we utilize the same approach. We also note that the Navier-Stokes equations (rather than the Euler equations) are often used for low Mach flow calculations; however, for the numerical tests presented here, the mesh resolution is so low that the kinematic viscosity coefficient appearing in the Navier-Stokes

equations is negligible, and consequently algorithms for either sets of equations will produce similar results.

To highlight the applicability of our noise reduction algorithm to RT problems, we shall artificially generate noise in the solution by using explicit forward Euler time integration, rather than the usual third order Runge-Kutta method used for the other test problems. As we shall show in §12.2.2, the use of the explicit first order in time method results in the generation of spurious high frequency oscillations in solutions computed without any noise reduction algorithm. This test allows us to model a typical scenario in computational physics, in which high resolution and long time simulations require the use of an extremely small Δt and, consequently, a prohibitively large number of time steps. Our aim is to show that the noise generated by using a larger time step (or lower order time integration method) can be removed by means of our noise algorithm, resulting in a noise-free and accurate solution.

Numerical simulations of the RT instability often suffer from the development of spurious small-scale structure due to the discretization of the problem (to be described in more detail below); see [13] for example. On the one hand, as described in [13], the numerical methods with the least amount of implicit diffusion, such as the Piecewise Parabolic Method (PPM), Virginia Hydrodynamics 1 (VH1) and WENO schemes, produce interface break-up at early times which corrupts the solution (even if the initial density and pressure are smoothed over a few cells). The solutions produced using these schemes generally do not possess the classical mushroom-shaped profile; the spurious small-scale structures give rise to a complex interface and a significant amount of mixing. On the other hand, the more dissipative methods in [13], such as the scheme of Liu and Lax (LL) and the CFLF hybrid (CFLFh) scheme, suppress this small-scale spurious structure from developing but, in doing so, produce solutions with overly smeared interfaces and overly diffused mixing zones with very little KH roll-up.

Our aim, therefore, is to produce a noise-free solution with a sharp interface and the classical mushroom-shaped profile, while ensuring that the KH-driven roll-up regions are not significantly affected. We do so by implementing the *anisotropic* version of the C -method (that we detail below).

12.1 Tangential spikes and the need for anisotropic diffusion

We now consider numerical simulations of the RT problem with data given by (31). Let us motivate the need for strictly tangential artificial viscosity operators for the long-time motion of contact discontinuities. In Fig.20, we show results of RT simulations, run with our simplified WENO scheme (without the use of any artificial viscosity); due to interpolation errors of the cosine function onto the uniform mesh, together with a lack of artificial viscosity, extremely large *tangential spikes* are produced in the vertical velocity, shown in Fig.20(a). These oscillations are, of course, non-physical. The interpolation error is demonstrated in Fig.20(b); the initial density profile has a tangential “staircase” whose jumps produce the tangential spikes in the vertical velocity, which in turn cause the interface to develop thin fingers as shown in Fig.20(c). The fingers continue to grow and, in the absence of any artificial diffusion, eventually interact with each other and corrupt the solution as shown in Fig.20(d).

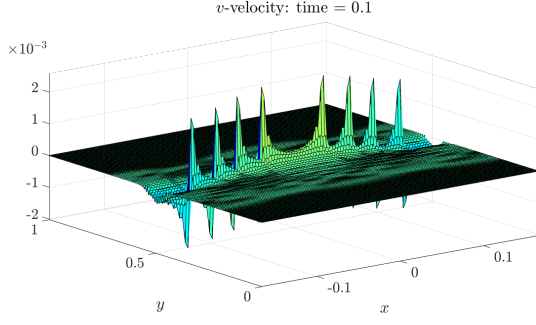
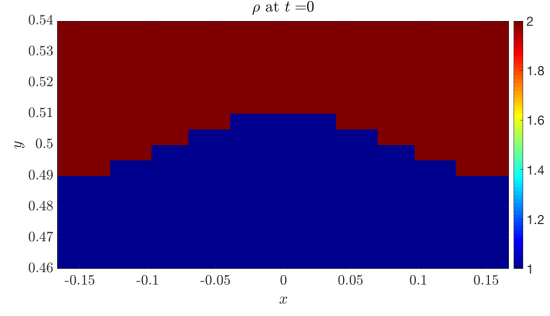
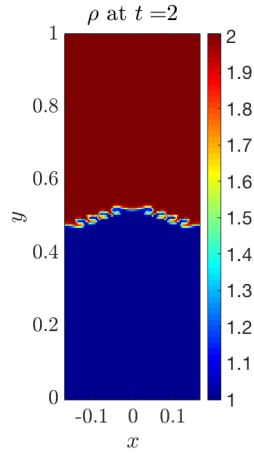
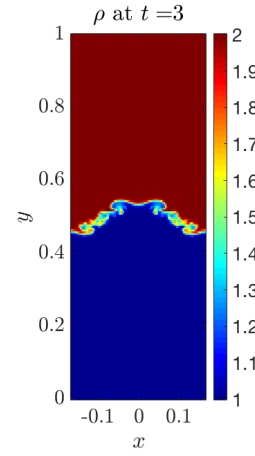

 (a) tangential spikes in the vertical velocity v .

 (b) “jumps” in the initial data for the density ρ . Figure is zoom-in on the initial interface Γ_0 .

 (c) development of fingers, caused by tangential spikes. Shown is a heatmap of the density ρ .

 (d) mixing caused by interaction between fingers. Shown is a heatmap of the density ρ .

Figure 20: Figures demonstrating the occurrence of tangential spikes due to the discretization of the initial conditions, which leads to the development of fingers and subsequent mixing. The solution is computed on a 50×200 grid on $[0, 1/6] \times [0, 1]$ using stand-alone WENO i.e. without any artificial diffusion.

Liska and Wendroff [13] smooth the initial density and pressure functions over a region of width $\mathcal{O}(\delta y)$ in the vertical direction; using smoothed initial data mitigates the development of the tangential spikes (although not entirely), but has the undesirable effect of overly diffusing the contact discontinuity, and modifying wave speeds in a non-transient manner. Moreover, this smoothing is not enough to suppress the development of spurious small-scale structure for the highest order schemes with the least amount of numerical diffusion; in particular, as shown in [13], both WENO and PPM break-up the interface.

Our strategy, therefore, is to implement the explicit anisotropic diffusion term in (13) for use with our simplified WENO scheme. The tangential artificial viscosity operators smooth the solution only in tangential directions with no diffusion added in directions normal to the contact curve. This is extremely important for RT problems which take a very long time to fully develop (for example, in the runs presented here, 425,000 time-steps are used for the numerical simulation). The equations of motion are thus given by the Euler- C^τ system (13)

with the addition of the gravity term $\mathbf{f} = [0, 0, -g\rho, -g\rho v]^T$ to the right-hand side of the equations.

Fig.21(a) and Fig.21(b) show the effect of tangential artificial viscosity: the contact discontinuity remains sharp, while the spurious tangential spikes are suppressed.

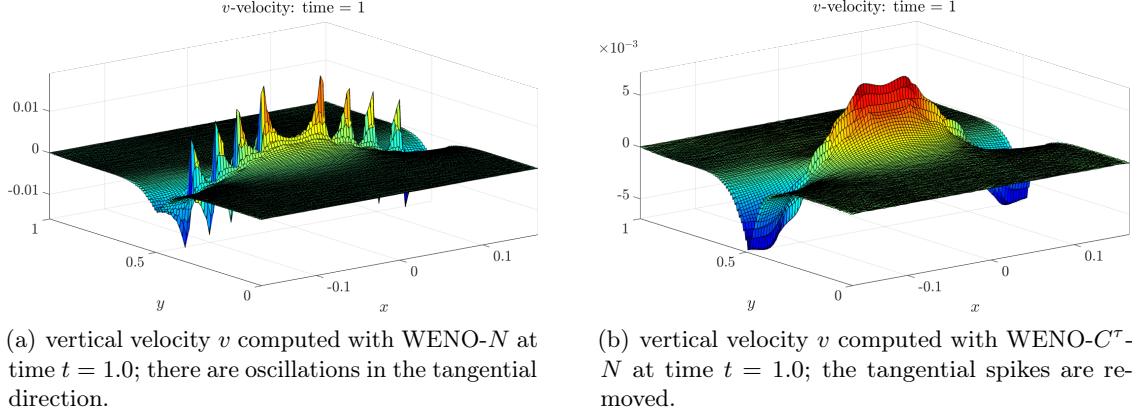


Figure 21: Demonstration of the removal of tangential spikes using anisotropic diffusion. Solutions are computed using WENO- N and WENO- C^τ - N in the domain $[0, 1/6] \times [0, 1]$ with 50×200 cells.

12.1.1 Boundary conditions for the RT problem

We implement reflecting boundary conditions for the RT problem on all four boundaries. Let $\vec{\nu}$ denote the normal vector to the boundary $\partial\Omega$. The reflecting boundary condition mean that $\vec{\nu} \cdot \mathbf{u}|_{\partial\Omega} = 0$ for all time $t \geq 0$. In the numerical discretization of the problem, this condition is enforced through the choice of *ghost node* values via an even or odd extension of each of the conservative variables. We provide further details in Appendix A.4, but mention here that the presence of the gravity terms in (13) requires that the pressure be extended in a linear fashion at the top and bottom boundaries so as to ensure that the vertical velocity v satisfies $v = 0$ there.

12.2 Application of WENO- C^τ - N to the RT instability

We now apply the WENO- C^τ - N scheme (detailed in Appendix A.3) to the RT instability. The domain $[0, 1/6] \times [0, 1]$ is discretized using a 50×200 cell grid with a time-step of $\delta t = 2 \times 10^{-5}$, and the problem is run up to a final time of $t = 8.5$. The artificial viscosity parameter in (14) is set as $\beta = 20.0$, the C -equation parameters are chosen as $\varepsilon = 0.4$ and $\kappa = 10.0$, and we employ our noise detection and removal algorithm, with $\delta h = 2 \times 10^{-5}$ in (19), $\delta_{\text{off}} = 0.05$ in (18), the noise removal viscosity η in (21) chosen such that $\eta \cdot \delta\tau / |\delta\mathbf{x}|^2 = 5 \times 10^{-4}$, and the local heat equation solver iterated for only a single time-step.

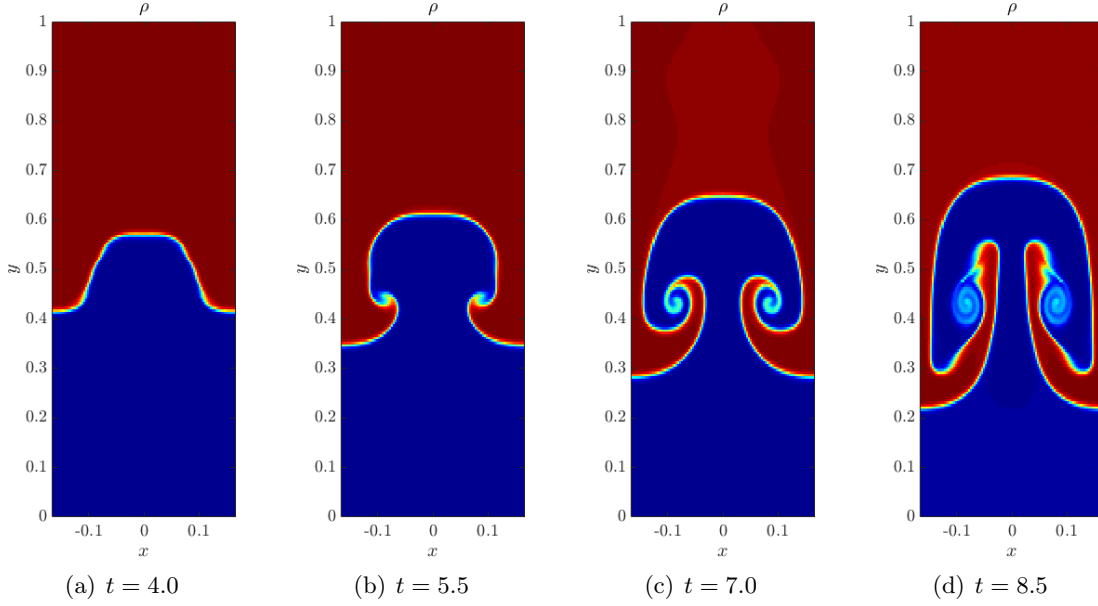


Figure 22: Application of WENO- C^τ - N to the RT instability in the domain $[0, 1/6] \times [0, 1]$ with 50×200 cells; figures are heatmap plots of the density ρ at various instances of time.

The density heatmap at various instances of time are presented in Fig.22. At time $t = 4.0$, the anisotropic diffusion acting in the tangential direction to the interface Γ prevents grid noise from developing into fingers and corrupting the solution, while ensuring that the interface Γ itself remains sharp, see Fig.22(a). By time $t = 5.5$, the solution begins to assume the classical “mushroom”-shaped profile (Fig.22(b)), and at time $t = 7.0$, the roll-up begins to occur, see Fig.22(c). The anisotropic diffusion ensures that the solution in the roll-up region does not become overly diffused, and this is demonstrated in Fig.22(d). This final figure should be compared with those figures in [13], which were produced with a finer mesh of 100×400 cells.

The WENO- C^τ - N solution shown in Fig.22 compares very favorably with those in [13], which are either overly diffused (such as LL, CFLFh), or are corrupted by the small-scale structure at the interface (PPM, VH1). We note here that low resolution simulations generally exhibit a significant amount of mixing due to numerical diffusion [2]. This is in contrast with the results presented here, where the low resolution 50×200 WENO- C^τ - N simulation produces a solution with a sharper interface and more development in the roll-up region than the solutions obtained from the high resolution 100×400 simulations in [13].

12.2.1 Comparison with isotropic artificial viscosity

If we instead use isotropic artificial viscosity, we cannot produce an RT simulation which is as good as that produce by the anisotropic scheme. Fig.23 shows the density profile for the RT simulation using the *isotropic* C -method as described by the Euler- C system (8) with $\beta^E = 0$ and $\beta^u = \beta^v = \beta$ with four different values of β .

The choice of $\beta = 1.0$ is insufficient to smooth the density oscillations in the tangential

direction, so that the fingers develop, interact with each other and eventually corrupt the solution. Setting $\beta = 5.0$ removes the density oscillations and produces a solution that is closer to the classic mushroom-shaped profile, but still results in a depression at the top of the mushroom. Moreover, there is very little roll-up occurring, as can be seen from Fig.23(b). Increasing to $\beta = 10.0$ removes the depression at the top of the mushroom, but results in almost no roll-up, see Fig.23(c). In Fig.23(d), we show the result computed with $\beta = 20.0$, which is the value of β used for the anisotropic C -method simulation shown Fig.22. The isotropic solution with $\beta = 20$ shows no roll-up at all.

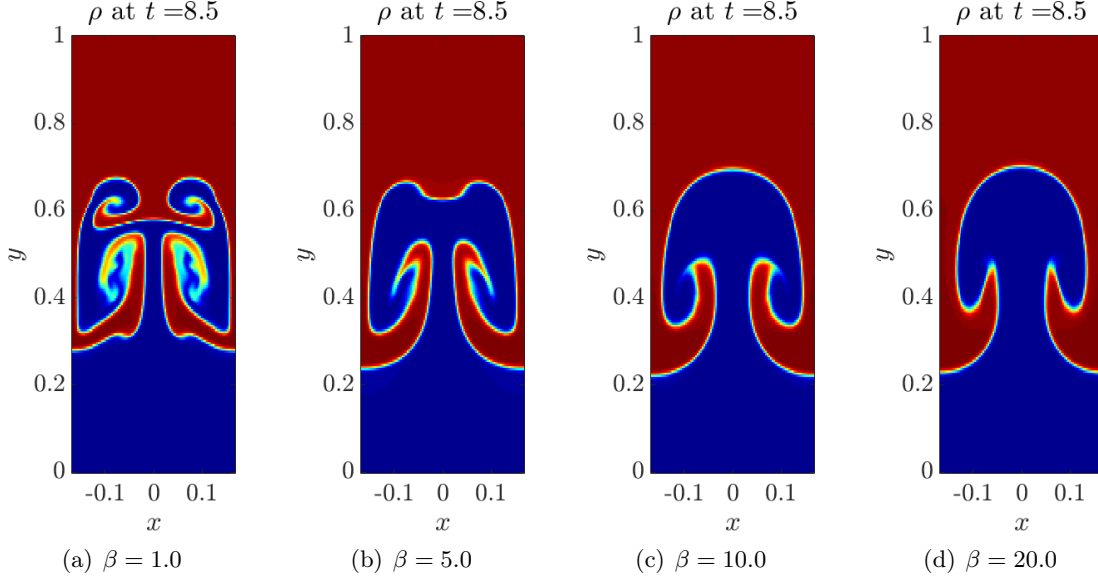


Figure 23: Application of WENO- C - N to the RT instability in $[0, 1/6] \times [0, 1]$ with 50×200 cells; figures are of the density ρ at the final time $t = 8.5$.

In Fig.24, we compute the L^q norm (with $q = 1, 2$) of the *vorticity* $\omega := \partial_x v - \partial_y u$, which is a measure of the local rotation of the fluid, and hence provides a measure of the amount of interface roll-up in the flow. It is evident that the solution computed with the anisotropic C -method displays the largest growth (in time) of the norm $\|\omega(\cdot, \cdot, t)\|_{L^q(\Omega)}$. The simulation with isotropic diffusion and $\beta = 1.0$ has a distinct increase in $\|\omega(\cdot, \cdot, t)\|_{L^1(\Omega)}$ at around time $t = 4.5$. This is due to the fingers that develop and roll-up; the growth then slows down due to the interaction between the fingers which causes mixing. The isotropic $\beta = 5.0$, $\beta = 10.0$ and $\beta = 20.0$ simulations share similar profiles for $\|\omega(\cdot, \cdot, t)\|_{L^q(\Omega)}$, with all three displaying significantly less growth of vorticity than the simulation run using WENO- C^τ - N .

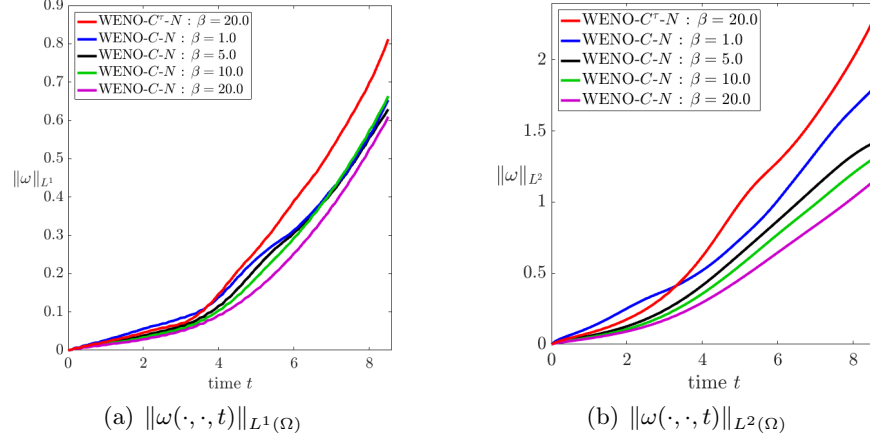


Figure 24: Comparison of the L^1 and L^2 norms of vorticity ω for solutions computed with anisotropic or isotropic diffusion.

12.2.2 Suppression of noise with the noise detection and removal algorithm

In this section, we briefly discuss the role of the noise detection and removal algorithm described in §6 in suppressing noise that would otherwise occur and corrupt the solution. In Fig.25, we compare the results from two simulations: one run using WENO- C^τ - N , which includes the noise detection and removal algorithm, and one run using WENO- C^τ , which does not include the noise detection and removal algorithm. The figures shown are of the horizontal velocity u at time $t = 1.0$. We recall that explicit forward Euler time integration is used for both simulations.

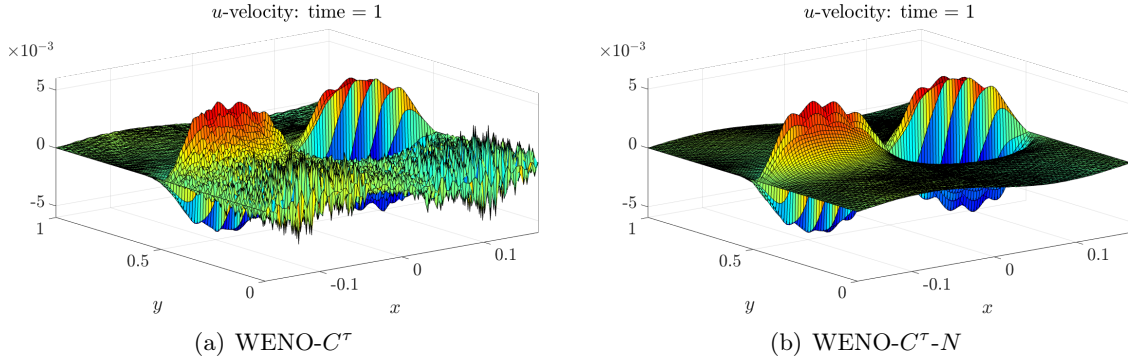
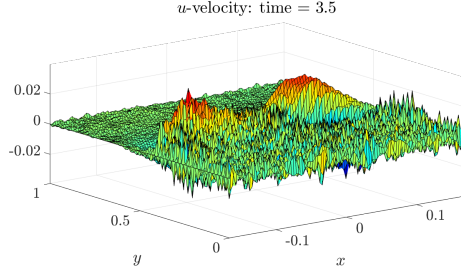


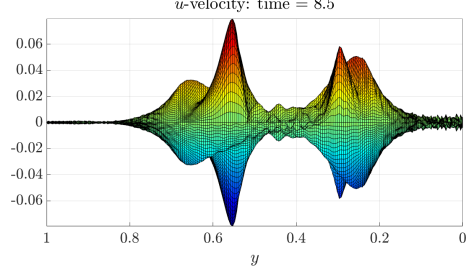
Figure 25: Figures demonstrating the ability of the wavelet-based noise detection and removal algorithm to suppress high-frequency spurious noise that can occur in the solution. Figures are of the horizontal velocity u . Fig.25(a) shows the solution computed with WENO- C^τ , while Fig.25(b) shows the solution computed with WENO- C^τ - N . Both solutions were solved in $[0, 1/6] \times [0, 1]$ with 50×200 cells and explicit forward Euler time integration, and are shown at time $t = 1.0$.

It is clear that the WENO- C^τ - N solution is much better than the WENO- C^τ solution.

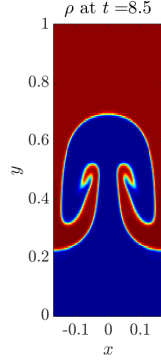
The noise that develops⁵ corrupts the WENO- C^τ solution at time $t = 1.0$, as shown in Fig.25(a). This is in contrast to the WENO- C^τ - N solution, which remains noise-free. We note here that the WENO- C^τ - N solution is unaffected at the interface Γ , due to the deactivation of the noise detection near the interface.



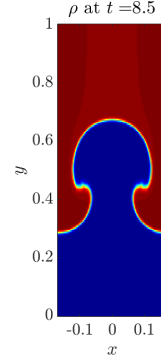
(a) $\beta_l = 1.0$: noise develops at early times. Shown is the horizontal velocity u



(b) $\beta_l = 2.0$: noise develops at late times, particularly near the bottom boundary $y = 0$; shown is a cross-section of the horizontal velocity u along $x = 0$



(c) $\beta_l = 3.0$: heatmap plot of the density ρ



(d) $\beta_l = 25.0$: heatmap plot of the density ρ

Figure 26: Figures showing solutions computed with linear viscosity replacing the noise detection and removal algorithm. Solutions computed in $[0, 1/6] \times [0, 1]$ with 50×200 cells using WENO- C^τ and a linear viscosity term to suppress the noise.

For the purpose of benchmarking our noise detection and removal procedure, we compare the algorithm with a simple alternative, namely the addition of a linear viscosity term to the right-hand side of the momentum equations (13b) and (13c) of the form

$$\beta_l |\delta \mathbf{x}|^2 \Delta \mathbf{u}, \quad (33)$$

⁵The use of explicit forward Euler time-stepping to simulate low Mach flow results in extremely severe stability constraints and, although the CFL condition is not violated, solutions are quickly corrupted by high-frequency noise.

with β_l the linear viscosity parameter. The resulting scheme is referred to as the WENO- C^τ - $\Delta \mathbf{u}$ scheme.

Setting $\beta_l = 25.0$ corresponds to the choice of $\eta \cdot \delta\tau / |\delta \mathbf{x}|^2 = 5 \times 10^{-4}$, which is the value used for the simulation shown in Fig.22. We present in Fig.26 the solutions obtained when the noise detection and removal algorithm is replaced by the linear viscosity (33), with various choices of β_l .

The issue with the uniform application of linear viscosity (33) is that the parameter β_l controlling the amount of diffusion needs to be large enough so as to suppress noise, while simultaneously small enough to allow some physical structure to develop in the KH mixing zones. For the RT problem considered here, this is not possible; for instance, the simulation run with $\beta_l = 25.0$, shown in Fig.26(d), is overly diffused with no structure at all in the roll-up region. The same is true, albeit to a lesser extent, with the choice of $\beta_l = 3.0$, shown in Fig.26(c). On the other hand, setting β_l too small by choosing, for example, $\beta_l = 1.0$ means that there is not enough viscosity to suppress the high frequency oscillations. This is demonstrated in Fig.26(a). The same is true, again to a lesser extent, when β_l is set as $\beta_l = 2.0$, see Fig.26(b). In this case, the noise is suppressed at the early stages, but begins to develop near the boundaries at later times, and again corrupts the solution. On the other hand, the use of the noise detection and removal algorithm allows for the use of a large amount of viscosity, due to the localized nature of the heat equation solver. The solution produced is noise-free, does not require the use of a smaller time-step, and retains the physical structure in the KH roll-up regions.

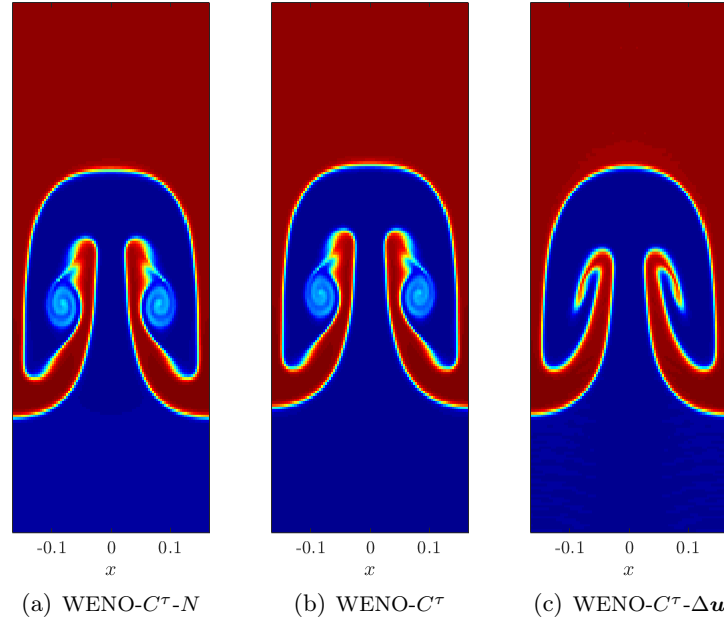
To quantitatively demonstrate the improvement in accuracy, we compare the solutions shown above with a “reference” solution \mathbf{U}^* . This reference solution is computed using WENO- C^τ with 50×200 cells and explicit third order Runge-Kutta time integration; the use of a higher order in time method results in a noise-free solution. We define the L^1 error norm of a computed quantity f as

$$E_f(t) = \Delta x \cdot \Delta y \sum_{i=1}^M \sum_{j=1}^N |f(x_i, y_j, t) - f^*(x_i, y_j, t)|, \quad (34)$$

where f^* is the reference solution, and M and N are the number of cells in the x and y directions, respectively. For this test, $M = 50$ and $N = 200$.

In Table 4, we provide $E_\rho(t)$, $E_u(t)$, and $E_v(t)$ at various times t for solutions computed using either WENO- C^τ , WENO- C^τ - N , or WENO- C^τ - $\Delta \mathbf{u}$. We see that the WENO- C^τ - N method produces solutions with smaller errors in all of the quantities and at each of the times t , which establishes the high accuracy of the method. Finally, we compare in Fig.27 WENO- C^τ - N with WENO- C^τ - $\Delta \mathbf{u}$ for $\beta_l = 2$, which is the optimal artificial viscosity parameter value for the linear viscosity scheme. It is clear from the figure that the WENO- C^τ - N solution is much closer in appearance to the reference solution than the WENO- C^τ - $\Delta \mathbf{u}$ solution is; the latter solution is overly smeared in the mixing regions due to the uniform application of viscosity, whereas the former solution retains the KH roll-up and matches almost exactly with the reference solution. These qualitative and quantitative observations establish the superiority of the noise detection and removal algorithm over the simple linear viscosity method.

| Error | Scheme | Time | | |
|-------------|---|------------------------|------------------------|------------------------|
| | | 3.0 | 7.0 | 8.5 |
| $E_\rho(t)$ | WENO- C^τ - N | 1.066×10^{-4} | 6.286×10^{-3} | 9.180×10^{-3} |
| | WENO- C^τ | 5.812×10^{-3} | fail | fail |
| | WENO- C^τ - $\Delta \mathbf{u}$: $\beta_t = 1.0$ | 3.914×10^{-4} | 8.033×10^{-3} | fail |
| | WENO- C^τ - $\Delta \mathbf{u}$: $\beta_t = 2.0$ | 4.475×10^{-4} | 6.349×10^{-3} | 9.222×10^{-3} |
| | WENO- C^τ - $\Delta \mathbf{u}$: $\beta_t = 3.0$ | 5.694×10^{-4} | 7.197×10^{-3} | 9.479×10^{-3} |
| | WENO- C^τ - $\Delta \mathbf{u}$: $\beta_t = 25.0$ | 1.852×10^{-3} | 2.238×10^{-2} | 2.952×10^{-2} |
| $E_u(t)$ | WENO- C^τ - N | 1.938×10^{-5} | 5.753×10^{-4} | 8.094×10^{-4} |
| | WENO- C^τ | 5.569×10^{-3} | fail | fail |
| | WENO- C^τ - $\Delta \mathbf{u}$: $\beta_t = 1.0$ | 1.302×10^{-4} | 2.691×10^{-3} | fail |
| | WENO- C^τ - $\Delta \mathbf{u}$: $\beta_t = 2.0$ | 6.694×10^{-5} | 6.013×10^{-4} | 8.819×10^{-4} |
| | WENO- C^τ - $\Delta \mathbf{u}$: $\beta_t = 3.0$ | 7.921×10^{-5} | 6.205×10^{-4} | 9.393×10^{-4} |
| | WENO- C^τ - $\Delta \mathbf{u}$: $\beta_t = 25.0$ | 2.040×10^{-4} | 1.085×10^{-3} | 1.160×10^{-3} |
| $E_v(t)$ | WENO- C^τ - N | 8.603×10^{-5} | 1.046×10^{-3} | 1.355×10^{-3} |
| | WENO- C^τ | 4.794×10^{-3} | fail | fail |
| | WENO- C^τ - $\Delta \mathbf{u}$: $\beta_t = 1.0$ | 2.469×10^{-4} | 2.776×10^{-3} | fail |
| | WENO- C^τ - $\Delta \mathbf{u}$: $\beta_t = 2.0$ | 1.015×10^{-4} | 1.109×10^{-3} | 1.480×10^{-3} |
| | WENO- C^τ - $\Delta \mathbf{u}$: $\beta_t = 3.0$ | 1.137×10^{-4} | 1.172×10^{-3} | 1.587×10^{-3} |
| | WENO- C^τ - $\Delta \mathbf{u}$: $\beta_t = 25.0$ | 2.651×10^{-4} | 2.253×10^{-3} | 2.820×10^{-3} |

Table 4: L^1 error analysis for the RT problem at various times t .**Figure 27:** Comparison of (a) WENO- C^τ - N , (b) WENO- C^τ with 3rd order Runge-Kutta, and (c) WENO- C^τ - $\Delta \mathbf{u}$ with $\beta_t = 2.0$. Figures are of the density ρ at the final time $t = 8.5$.

13 Concluding remarks

This paper presents the two-dimensional generalization of the 1- D C -method described in [18]. The 2- D C -method is a space-time smooth artificial viscosity scheme for adding *isotropic* diffusion to shock curves and *anisotropic* diffusion to contact discontinuities. We have applied the isotropic C -method to four difficult problems, namely the Noh problem, the Sedov point blast test, the Sod circular explosion problem, and the Mach 10 reflection test, and demonstrated that our method compares favorably to stand-alone WENO as well as the WENO-Noh scheme, the latter using the artificial viscosity method of Noh [15].

We have also demonstrated the efficacy of the anisotropic C -method. For problems requiring long-time evolution of contact discontinuities with hundreds of thousands of time-steps, the *anisotropic* C -method works extremely well. This method was applied to the RT instability problem of Liska-Wendroff [13], and was shown to be able to suppress tangential spikes, while keeping the interface sharp and not overly diffusing the KH roll-up regions.

For problems with shock-contact interaction, our C -method uses a C -function to track the shock and another \hat{C} -function to track the contact discontinuity. These two functions interact with one another: when the shock interacts with the contact, the C tracking the shock goes to zero, allowing the \hat{C} of the contact to stabilize the contact curve without dissipation from the shock front.

We have also described a simple shock-wall collision scheme for stabilizing shock fronts during wall collision and bounce-back, and demonstrated its ability to suppress post-collision noise for a Sod-type explosion problem and the double Mach 10 reflection test.

For high-frequency noise detection and removal, we have devised and implemented a simple 2- D wavelet-based scheme for detecting these oscillations followed by a highly localized (in both space and time) removal algorithm based on a local explicit heat equation solver. This noise detection and removal scheme has been applied to the RT and Noh problems, wherein it suppressed high-frequency noise while retaining sharp shock and contact fronts.

The qualitative and quantitative observations presented in this paper, together with the extensive accuracy studies presented in [18] in the 1- D case, indicate that the schemes are high-order and produce accurate solutions, even with the use of our highly simplified finite-difference WENO method.

A Numerical discretization and schemes

In this section, we provide details for the WENO-based schemes used to produce the results in this paper. We first describe the simplified WENO procedure used for the spatial discretization of the nonlinear flux terms in the Euler equations. We then describe the implementation for the Euler- C and Euler- C^τ systems.

For readability, we will use Table 5 to refer to these various schemes.

| Scheme | Description |
|--|--|
| WENO | standard fifth-order WENO procedure for the usual Euler equations (1). |
| WENO-Noh | WENO scheme with Noh's artificial viscosity method (24). |
| WENO- C | WENO scheme with the <i>isotropic</i> C -method (8). |
| WENO- C^τ | WENO scheme with the <i>anisotropic</i> C -method (13). |
| WENO- C - N and WENO- C^τ - N | WENO- C and WENO- C^τ with the noise detection and removal algorithm described in §6. |
| WENO- C - \hat{C} | WENO scheme with the <i>isotropic</i> C -method for shock fronts and the <i>anisotropic</i> C -method for contact discontinuities (see §10.1). |
| WENO- C - W | WENO scheme with the shock-wall collision scheme (15). |

Table 5: Various numerical schemes used in the simulations.

A.1 WENO reconstruction procedure

Our WENO reconstruction procedure is formally fifth-order with upwinding performed based only on the sign of the velocity at the cell edges. In particular, no approximate Riemann solvers are used.

The spatial domain $\Omega = [x_1, x_M] \times [y_1, y_N]$ is subdivided into $M \cdot N$ cells, each with area $\delta x \cdot \delta y$. We employ the notation

$$x_{i+\frac{1}{2}} = \frac{x_i + x_{i+1}}{2} \quad \text{and} \quad y_{j+\frac{1}{2}} = \frac{y_j + y_{j+1}}{2}.$$

Any quantity w evaluated at a cell center (x_i, y_j) shall be denoted by $w_{i,j}$. Similarly, any quantity w evaluated at the center of the cell edge $(x_{i\pm\frac{1}{2}}, y_j)$ shall be denoted by $w_{i\pm\frac{1}{2},j}$, and at the cell edge $(x_i, y_{j\pm\frac{1}{2}})$ by $w_{i,j\pm\frac{1}{2}}$. The quantity w evaluated at the cell corners $(x_{i\pm\frac{1}{2}}, y_{j\pm\frac{1}{2}})$ is denoted by $w_{i\pm\frac{1}{2},j\pm\frac{1}{2}}$.

Given an array $(a_{r,s})$ corresponding to cell-center values of the quantity a , and arrays $f_{r\pm\frac{1}{2},s}$ and $g_{r,s\pm\frac{1}{2}}$ corresponding to cell-edge values of the quantities f and g , respectively, we define the $(i,j)^{\text{th}}$ component of the array $\text{WENO} \left(a_{r,s}, f_{r\pm\frac{1}{2},s}, g_{r,s\pm\frac{1}{2}} \right)$ by

$$\left[\text{WENO} \left(a_{r,s}, f_{r\pm\frac{1}{2},s}, g_{r,s\pm\frac{1}{2}} \right) \right]_{i,j} = \left[\text{WENO}_x \left(a_{r,s}, f_{r\pm\frac{1}{2},s} \right) \right]_{i,j} + \left[\text{WENO}_y \left(a_{r,s}, g_{r,s\pm\frac{1}{2}} \right) \right]_{i,j},$$

with

$$\begin{aligned} \left[\text{WENO}_x \left(a_{r,s}, f_{r,\pm\frac{1}{2},s} \right) \right]_{i,j} &= \frac{1}{\delta x} \left(\tilde{a}_{i+\frac{1}{2},j} f_{i+\frac{1}{2},j} - \tilde{a}_{i-\frac{1}{2},j} f_{i-\frac{1}{2},j} \right) \\ \left[\text{WENO}_y \left(a_{r,s}, g_{r,s,\pm\frac{1}{2}} \right) \right]_{i,j} &= \frac{1}{\delta y} \left(\tilde{a}_{i,j+\frac{1}{2}} g_{i,j+\frac{1}{2}} - \tilde{a}_{i,j-\frac{1}{2}} g_{i,j-\frac{1}{2}} \right), \end{aligned}$$

where the cell-edge values $\tilde{a}_{i\pm\frac{1}{2},j}$ and $\tilde{a}_{i,j\pm\frac{1}{2}}$ are calculated using a standard fifth-order WENO reconstruction procedure (see [8, 26]) with upwinding performed based on the sign of $f_{i\pm\frac{1}{2},j}$ and $g_{i,j\pm\frac{1}{2}}$, respectively.

Then, defining the vector $\mathbf{U} = [\rho, \rho u, \rho v, E]^T$, we construct the operator $\mathcal{F}_{\text{WENO}}$ as

$$[\mathcal{F}_{\text{WENO}}(\mathbf{U}_{r,s})]_{i,j} = - \begin{bmatrix} \left[\text{WENO} \left(\rho_{r,s}, \hat{u}_{r,\pm\frac{1}{2},s}, \hat{v}_{r,s,\pm\frac{1}{2}} \right) \right]_{i,j} \\ \left[\text{WENO} \left((\rho u)_{r,s}, \hat{u}_{r,\pm\frac{1}{2},s}, \hat{v}_{r,s,\pm\frac{1}{2}} \right) \right]_{i,j} + \tilde{\partial}_{x,4} p_{i,j} \\ \left[\text{WENO} \left((\rho v)_{r,s}, \hat{u}_{r,\pm\frac{1}{2},s}, \hat{v}_{r,s,\pm\frac{1}{2}} \right) \right]_{i,j} + \tilde{\partial}_{y,4} p_{i,j} \\ \left[\text{WENO} \left((E+p)_{r,s}, \hat{u}_{r,\pm\frac{1}{2},s}, \hat{v}_{r,s,\pm\frac{1}{2}} \right) \right]_{i,j} \end{bmatrix}.$$

Here, we use the notation $\tilde{\partial}_{x,4} p_{i,j}$ and $\tilde{\partial}_{y,4} p_{i,j}$ to denote the fourth-order central difference approximation for $\partial_x p$ and $\partial_y p$, respectively, at the cell-center (x_i, y_j) . The cell-edge velocities $\hat{u}_{i\pm\frac{1}{2},j}$ and $\hat{v}_{i,j\pm\frac{1}{2}}$ are calculated using a fourth-order averaging:

$$\begin{aligned} \hat{u}_{i-\frac{1}{2},j} &= \frac{-u_{i-2,j} + 7u_{i-1,j} + 7u_{i,j} - u_{i+1,j}}{12}, \\ \hat{v}_{i,j-\frac{1}{2}} &= \frac{-v_{i,j-2} + 7v_{i,j-1} + 7v_{i,j} - v_{i,j+1}}{12}. \end{aligned}$$

The operator $\mathcal{F}_{\text{WENO}}$ provides the discretization of the nonlinear flux terms in the Euler systems (1), (8), (13) and (15). Below, we describe the discretization and implementation of the various forms of artificial viscosity used in this paper. If no artificial viscosity is implemented, then we have the semi-discrete equations

$$\frac{d}{dt} \mathbf{U}_{i,j} = [\mathcal{F}_{\text{WENO}}(\mathbf{U}_{r,s})]_{i,j}$$

corresponding to the Euler system (1). Given the solution at a time-step $t_n = n \cdot \delta t$, denoted by $\mathbf{U}_{i,j}^n$, time integration is done using an explicit k^{th} order Runge-Kutta method:

$$\mathbf{U}_{i,j}^{n+1} = \text{RK}(\mathbf{U}_{i,j}^n, [\mathcal{F}_{\text{WENO}}(\mathbf{U}_{r,s}^n)]_{i,j}; k). \quad (35)$$

We will refer to the scheme (35) as “WENO”, or “stand-alone WENO”.

A.2 The WENO- C and WENO- C - N schemes

We first describe the discretization of the Euler- C system (8). Given arrays $(w_{r,s})$, $(C_{r,s})$ and $(\rho_{r,s})$ corresponding to cell-center values of the quantities w , C and ρ , and a time-dependent function $\tilde{\beta}$, the $(i, j)^{\text{th}}$ component of the array $\text{DIFF}(w_{r,s}, C_{r,s}, \rho_{r,s}; \tilde{\beta})$ is defined as

$$\begin{aligned} \left[\text{DIFF}(w_{r,s}, C_{r,s}, \rho_{r,s}; \tilde{\beta}) \right]_{i,j} &:= \frac{\tilde{\beta}}{\delta x} \left(\rho_{i+\frac{1}{2},j} C_{i+\frac{1}{2},j} \tilde{\partial} w_{i+\frac{1}{2},j} - \rho_{i-\frac{1}{2},j} C_{i-\frac{1}{2},j} \tilde{\partial} w_{i-\frac{1}{2},j} \right) \\ &\quad + \frac{\tilde{\beta}}{\delta y} \left(\rho_{i,j+\frac{1}{2}} C_{i,j+\frac{1}{2}} \tilde{\partial} w_{i,j+\frac{1}{2}} - \rho_{i,j-\frac{1}{2}} C_{i,j-\frac{1}{2}} \tilde{\partial} w_{i,j-\frac{1}{2}} \right), \end{aligned}$$

where

$$\tilde{\partial} w_{i+\frac{1}{2},j} = \frac{w_{i+1,j} - w_{i,j}}{\delta x} \quad \text{and} \quad \tilde{\partial} w_{i,j+\frac{1}{2}} = \frac{w_{i,j+1} - w_{i,j}}{\delta y},$$

and the notation $z_{i\pm\frac{1}{2},j}$ and $z_{i,j\pm\frac{1}{2}}$ denote the quantity evaluated at the cell edges $(x_{i\pm\frac{1}{2}}, y_j)$ and $(x_i, y_{j\pm\frac{1}{2}})$, respectively, using a standard averaging e.g.

$$z_{i+\frac{1}{2},j} = \frac{z_{i+1,j} + z_{i,j}}{2}.$$

The operator $\mathcal{D}_{\text{DIFF}}$ is then defined by

$$[\mathcal{D}_{\text{DIFF}}(\mathbf{U}_{r,s}, C_{r,s})]_{i,j} = \begin{bmatrix} 0 \\ \left[\text{DIFF}(u_{r,s}, C_{r,s}, \rho_{r,s}; \tilde{\beta}^u) \right]_{i,j} \\ \left[\text{DIFF}(v_{r,s}, C_{r,s}, \rho_{r,s}; \tilde{\beta}^u) \right]_{i,j} \\ \left[\text{DIFF}\left((E/\rho)_{r,s}, C_{r,s}, \rho_{r,s}; \tilde{\beta}^E\right) \right]_{i,j} \end{bmatrix},$$

where the artificial viscosity coefficients are given by (9).

We also define the operator $\mathcal{L}(C_{r,s}; \varepsilon, \kappa)$ by

$$[\mathcal{L}(C_{r,s}; \varepsilon, \kappa)]_{i,j} = \frac{S(\mathbf{u}_{r,s})}{\varepsilon |\delta \mathbf{x}|} ([G\rho]_{i,j} - C_{i,j}) + \kappa S(\mathbf{u}_{r,s}) |\delta \mathbf{x}| \left(\tilde{\partial} C_{i+\frac{1}{2},j} - \tilde{\partial} C_{i-\frac{1}{2},j} + \tilde{\partial} C_{i,j+\frac{1}{2}} - \tilde{\partial} C_{i,j-\frac{1}{2}} \right),$$

where $S(\mathbf{u}_{r,s})$ is given by (3).

The isotropic Euler- C system (8) is then approximated by the semi-discrete equations

$$\begin{cases} \frac{d}{dt} \mathbf{U}_{i,j} = [\mathcal{F}_{\text{WENO}}(\mathbf{U}_{r,s}) + \mathcal{D}_{\text{DIFF}}(\mathbf{U}_{r,s}, C_{r,s})]_{i,j}, \\ \frac{d}{dt} C_{i,j} = [\mathcal{L}(C_{r,s}; \varepsilon, \kappa)]_{i,j}, \end{cases}$$

and time integration is again done using a k^{th} order Runge-Kutta method:

$$\mathbf{U}_{i,j}^{n+1} = \text{RK} \left(\mathbf{U}_{i,j}^n, [\mathcal{F}_{\text{WENO}}(\mathbf{U}_{r,s}^n) + \mathcal{D}_{\text{DIFF}}(\mathbf{U}_{r,s}^n, C_{r,s}^n)]_{i,j}; k \right), \quad (36a)$$

$$C_{i,j}^{n+1} = \text{RK} \left(C_{i,j}^n, [\mathcal{L}(C_{r,s}^n; \varepsilon, \kappa)]_{i,j}; k \right). \quad (36b)$$

We will refer to the scheme (36) as the WENO- C scheme. When coupled with the noise detection and removal algorithm as detailed in §6.3, the scheme will be referred to as the WENO- C - N scheme.

A.3 The WENO- C^τ and WENO- C^τ - N schemes

Next, we describe the discretization procedure for the Euler- C^τ system (13). The anisotropic diffusion operator DIFF_τ is defined by

$$\begin{aligned} & \left[\text{DIFF}_\tau(w_{r,s}, C_{r,s}, C_{r,s}^{\tau_1}, C_{r,s}^{\tau_2}, \rho_{r,s}; \tilde{\beta}) \right]_{i,j} := \\ & \frac{\tilde{\beta}}{\delta x} \left(\rho_{i+\frac{1}{2},j} C_{i+\frac{1}{2},j} C_{i+\frac{1}{2},j}^{\tau_1} C_{i+\frac{1}{2},j}^{\tau_1} \tilde{\partial} w_{i+\frac{1}{2},j} - \rho_{i-\frac{1}{2},j} C_{i-\frac{1}{2},j} C_{i-\frac{1}{2},j}^{\tau_1} C_{i-\frac{1}{2},j}^{\tau_1} \tilde{\partial} w_{i-\frac{1}{2},j} \right) \\ & + \frac{\tilde{\beta}}{\delta y} \left(\rho_{i,j+\frac{1}{2}} C_{i,j+\frac{1}{2}} C_{i,j+\frac{1}{2}}^{\tau_2} C_{i,j+\frac{1}{2}}^{\tau_2} \tilde{\partial} w_{i,j+\frac{1}{2}} - \rho_{i,j-\frac{1}{2}} C_{i,j-\frac{1}{2}} C_{i,j-\frac{1}{2}}^{\tau_2} C_{i,j-\frac{1}{2}}^{\tau_2} \tilde{\partial} w_{i,j-\frac{1}{2}} \right) \\ & + \frac{\tilde{\beta}}{\delta x} \left(\rho_{i+\frac{1}{2},j} C_{i+\frac{1}{2},j} C_{i+\frac{1}{2},j}^{\tau_1} C_{i+\frac{1}{2},j}^{\tau_2} \hat{\partial} w_{i+\frac{1}{2},j} - \rho_{i-\frac{1}{2},j} C_{i-\frac{1}{2},j} C_{i-\frac{1}{2},j}^{\tau_1} C_{i-\frac{1}{2},j}^{\tau_2} \hat{\partial} w_{i-\frac{1}{2},j} \right) \\ & + \frac{\tilde{\beta}}{\delta y} \left(\rho_{i,j+\frac{1}{2}} C_{i,j+\frac{1}{2}} C_{i,j+\frac{1}{2}}^{\tau_1} C_{i,j+\frac{1}{2}}^{\tau_2} \hat{\partial} w_{i,j+\frac{1}{2}} - \rho_{i,j-\frac{1}{2}} C_{i,j-\frac{1}{2}} C_{i,j-\frac{1}{2}}^{\tau_1} C_{i,j-\frac{1}{2}}^{\tau_2} \hat{\partial} w_{i,j-\frac{1}{2}} \right), \end{aligned}$$

where $\hat{\partial} w_{i\pm\frac{1}{2},j}$ and $\hat{\partial} w_{i,j\pm\frac{1}{2}}$ are approximations to the derivatives $\partial_y w$ at $(x_{i\pm\frac{1}{2}}, y_j)$ and $\partial_x w$ at $(x_i, y_{j\pm\frac{1}{2}})$, respectively:

$$\begin{aligned} \hat{\partial} w_{i\pm\frac{1}{2},j} &= \frac{w_{i\pm\frac{1}{2},j+\frac{1}{2}} - w_{i\pm\frac{1}{2},j-\frac{1}{2}}}{\delta y}, \\ \hat{\partial} w_{i,j\pm\frac{1}{2}} &= \frac{w_{i+\frac{1}{2},j\pm\frac{1}{2}} - w_{i-\frac{1}{2},j\pm\frac{1}{2}}}{\delta x}. \end{aligned}$$

We use the notation $w_{i\pm\frac{1}{2},j\pm\frac{1}{2}}$ to mean the quantity w evaluated at the cell corner $(x_{i\pm\frac{1}{2}}, y_{j\pm\frac{1}{2}})$ using a simple averaging. For example,

$$w_{i+\frac{1}{2},j+\frac{1}{2}} = \frac{w_{i,j} + w_{i+1,j} + w_{i,j+1} + w_{i+1,j+1}}{4}.$$

Defining the vector $\mathbf{C} = [C, C^{\tau_1}, C^{\tau_2}]^\tau$, we construct the operator $\mathcal{D}_{\text{DIFF}}^\tau$ as

$$[\mathcal{D}_{\text{DIFF}}^\tau(\mathbf{U}_{r,s}, \mathbf{C}_{r,s})]_{i,j} = \begin{bmatrix} 0 \\ \left[\text{DIFF}_\tau(u_{r,s}, C_{r,s}, C_{r,s}^{\tau_1}, C_{r,s}^{\tau_2}, \rho_{r,s}; \tilde{\beta}) \right]_{i,j} \\ \left[\text{DIFF}_\tau(v_{r,s}, C_{r,s}, C_{r,s}^{\tau_1}, C_{r,s}^{\tau_2}, \rho_{r,s}; \tilde{\beta}) \right]_{i,j} \\ 0 \end{bmatrix},$$

where the artificial viscosity coefficient $\tilde{\beta}$ is defined by (14).

The anisotropic Euler- C^τ system (13) may then be approximated by the semi-discrete equations

$$\begin{cases} \frac{d}{dt} \mathbf{U}_{i,j} = [\mathcal{F}_{\text{WENO}}(\mathbf{U}_{r,s}) + \mathcal{D}_{\text{DIFF}}^\tau(\mathbf{U}_{r,s}, \mathbf{C}_{r,s})]_{i,j}, \\ \frac{d}{dt} \mathbf{C}_{i,j} = [\mathcal{L}(\mathbf{C}_{r,s}; \varepsilon, \kappa)]_{i,j}, \end{cases}$$

and time-integration is done using a k^{th} order Runge-Kutta solver:

$$\mathbf{U}_{i,j}^{n+1} = \text{RK} \left(\mathbf{U}_{i,j}^n, [\mathcal{F}_{\text{WENO}}(\mathbf{U}_{r,s}^n) + \mathcal{D}_{\text{DIFF}}^{\tau}(\mathbf{U}_{r,s}^n, \mathbf{C}_{r,s}^n)]_{i,j}; k \right), \quad (37a)$$

$$\mathbf{C}_{i,j}^{n+1} = \text{RK} \left(\mathbf{C}_{i,j}^n, [\mathcal{L}(\mathbf{C}_{r,s}^n; \varepsilon, \kappa)]_{i,j}; k \right). \quad (37b)$$

We refer to the anisotropic scheme (37) as the WENO- C^{τ} scheme or, when coupled with the noise detection and removal algorithm in §6.3, as the WENO- C^{τ} - N scheme.

A.4 Boundary conditions and ghost node values

In general, the boundary conditions for the various problems considered here are imposed through the assigning of values to the *ghost nodes*. Generally, either an even extension or an odd extension of the variable in question is employed. For our (formally) fifth-order WENO reconstruction procedure, 7 nodes in each direction are used to reconstruct the flux at a cell-center, so that three ghost node values are required in each direction. By an even extension at the left and right boundaries of the variable w , we mean that

$$w_{1-i,j} = w_{1+i,j} \quad \text{and} \quad w_{M+i,j} = w_{M-i,j} \quad \text{for } i = 1, 2, 3,$$

while an odd extension at the left and right boundaries means

$$w_{1-i,j} = -w_{1+i,j} \quad \text{and} \quad w_{M+i,j} = -w_{M-i,j} \quad \text{for } i = 1, 2, 3.$$

An analogous identity holds for the top and bottom boundaries.

A.4.1 Boundary conditions for the RT problem

The numerical solution to the Rayleigh-Taylor problem 12 is computed on the half-domain $[0, 1/6] \times [0, 1]$ and then reflected appropriately to yield the solution on all of $\Omega = [-1/6, 1/6] \times [0, 1]$. Consequently, reflecting boundary conditions are used on the left boundary $x = 0$ and right boundary $x = 1/6$. These are imposed through the ghost-node values; an even extension of ρ , E , ρv , C , and C^{τ_1} is imposed, while an odd extension of ρu and C^{τ_2} is enforced. At the top and bottom boundaries, ρ , ρu , C , C^{τ_1} , and C^{τ_2} are extended in an even fashion, ρv is extended in an odd fashion, and the pressure p is extended linearly so as to preserve hydrostatic equilibrium:

$$p_{i,1-j} = 2p_{i,1-j+1} - p_{i,1-j+2} \quad \text{and} \quad p_{i,N+j} = 2p_{i,N+j-1} - p_{i,N+j-2}$$

for $j = 1, 2, 3$ and $i = 1, \dots, M$.

Acknowledgements

Research reported in this publication was supported by the Office of Defense Nuclear Nonproliferation Research and Development and by the Defense Threat Reduction Agency under Interagency Agreement number HDTRA1825370 (DTRA10027 – 25370) as work for others. SS was partially supported by DTRA HDTRA11810022.

We would like to express our gratitude to the anonymous referees for their numerous suggestions that have greatly improved the manuscript.

References

- [1] H.A. Bethe, K. Fuchs, J.O. Hirschfelder, J.L. Magee, R.E. Peierls, & J. von Neumann. Blast Wave, *Los Alamos Scientific Laboratory Report LA-2000*, 1947. 9
- [2] A. C. Calder *et al.* On validating an astrophysical simulation code. *The Astrophysical Journal Supplement Series*, 143(1):201, 2002. 12.2
- [3] S. Chandrasekhar. *Hydrodynamic and Hydromagnetic Stability*. Dover Books on Physics Series. Dover Publications, 1961. 12
- [4] D. Coutand and S. Shkoller. On the finite-time splash and splat singularities for the 3-D free-surface Euler equations. *Comm. Math. Phys.*, 325(1):143–183, 2014. 1
- [5] P. Colella and P. R. Woodward. The numerical simulation of two-dimensional fluid flow with strong shocks. *Journal of Computational Physics*, 54:115 – 173, 1984. 11
- [6] M. Crandall and A. Majda. The method of fractional steps for conservation laws. *Numerische Mathematik*, 34:285–314, 1980. 1.1
- [7] C. Hu and C.-W. Shu. Weighted essentially non-oscillatory schemes on triangular meshes. *Journal of Computational Physics*, 150:97–127, 1999. 1.1
- [8] G.-S. Jiang and C.-W. Shu. Efficient implementation of weighted ENO schemes. *Journal of Computational Physics*, 126:202–228, 1996. 7.1, 4, A.1
- [9] G.-S. Jiang and E. Tadmor. Nonoscillatory central schemes for multidimensional hyperbolic conservation laws. *SIAM J. Sci. Comput*, 19:1892–1917, 1998. 1.1
- [10] J.R. Kamm. Evaluation of the Sedov-von Neumann-Taylor blast wave solution. *Technical Report LA-UR-00-6055*, Los Alamos National Laboratory, 2000. 9
- [11] James R. Kamm and F. X. Timmes. On efficient generation of numerically robust Sedov solutions. Technical report, 2007. 9
- [12] H. J. Kull. Theory of the Rayleigh-Taylor instability. *Physics Reports*, 206(5):197 – 325, 1991. 12, 12
- [13] R. Liska and B. Wendroff. Comparison of several difference schemes on 1D and 2D test problems for the Euler equations. *SIAM J. Sci. Comput*, 25:995–1017, 2003. (document), 7.1, 7.1, 8, 8, 8.1, 10, 10, 10.1, 12, 12, 12.1, 12.2, 13
- [14] D. Livescu. Compressibility effects on the rayleigh-taylor instability growth between immiscible fluids. *Physics of Fluids*, 16(1):118–127, 2004. 12
- [15] W. F Noh. Errors for calculations of strong shocks using an artificial viscosity and an artificial heat flux. *J. Comput. Phys.*, 72(1):78 – 120, 1987. 8, 8, 8.2, 13
- [16] J. J. Quirk. A contribution to the great Riemann solver debate. *Int. J. Num. Methods Fluids*, 18:555–574, 1994. 11

- [17] Lord Rayleigh. Investigation of the character of the equilibrium of an incompressible heavy fluid of variable density. *Proceedings of the London Mathematical Society*, s1-14(1):170–177, 1882. 12, 12
- [18] R. Ramani, J. Reisner, and S. Shkoller. A space-time smooth artificial viscosity method with wavelet noise indicator and shock collision scheme, Part 1: the 1-D case. *Preprint*, 2018. (document), 1, 1.1, 1.2, 1.3, 3.1, 3.1, 3.1, 5, 6, 6.1, 6.1, 6.2, 6.3, 1, 7, 8, 8.2, 13
- [19] R. Ramani, J. Reisner, and S. Shkoller. A space-time smooth artificial viscosity method for shock-shock and shock-contact collision. *In preparation*. 1.1, 2, 1
- [20] J. Reisner, J. Serencsa, and S. Shkoller. A space-time smooth artificial viscosity method for nonlinear conservation laws. *J. Comput. Phys.*, 235:912–933, 2013. (document), 1.1, 3.1, 3.1, 3.2
- [21] W. J. Rider. Revisiting wall heating. *J. Comput. Phys.*, 162(2):395 – 410, 2000. 1.3, 8
- [22] L. I. Sedov. The movement of air in a strong explosion. In *Dokl. Akad. Nauk SSSR*, volume 52, pages 17–20, 1946. 9
- [23] L. I. Sedov. *Similarity and dimensional methods in mechanics*. Translation by Morris Friedman (translation edited by Maurice Holt). Academic Press, New York-London, 1959. 9
- [24] D. H. Sharp. An overview of rayleigh-taylor instability. *Physica D: Nonlinear Phenomena*, 12(1):3 – 18, 1984. 12
- [25] Jing Shi, Yong-Tao Zhang, and Chi-Wang Shu. Resolution of high order weno schemes for complicated flow structures. *Journal of Computational Physics*, 186(2):690 – 696, 2003. 11
- [26] C.-W. Shu. High-order finite difference and finite volume weno schemes and discontinuous galerkin methods for cfd. *International Journal of Computational Fluid Dynamics*, 17(2):107–118, 2003. A.1
- [27] T. C. Sideris. Formation of singularities in three-dimensional compressible fluids. *Comm. Math. Phys.*, 101(4):475–485, 1985. 1
- [28] G. A. Sod. A survey of several finite difference methods for systems of nonlinear hyperbolic conservation laws. *Journal of Computational Physics*, 27:1 – 31, 1978. 10
- [29] J. M. Stone. The Athena Code Test Page. <https://www.astro.princeton.edu/~jstone/Athena/tests/>. Accessed: 12-17-2018. 4, 12
- [30] G. I. Taylor. The instability of liquid surfaces when accelerated in a direction perpendicular to their planes. i. *Proceedings of the Royal Society of London A: Mathematical, Physical and Engineering Sciences*, 201(1065):192–196, 1950. 12, 12

- [31] G. I. Taylor. The formation of a blast wave by a very intense explosion i. theoretical discussion. *Proceedings of the Royal Society of London. Series A. Mathematical and Physical Sciences*, 201(1065):159–174, 1950. 9
- [32] K. W. Thompson. Time-dependent boundary conditions for hyperbolic systems. *J. Comput. Phys.*, 68(1):1–24, 1987. 10
- [33] F. Timmes. Sedov blast wave verification problem. http://cococubed.asu.edu/research_pages/sedov.shtml. Accessed: 12-17-2018. 9
- [34] E. F. Toro. *Riemann solvers and numerical methods for fluid dynamics*. Springer-Verlay Berling Heidelberg, 2009. 10, 10
- [35] J. T. Waddell, C. E. Niederhaus, and J. W. Jacobs. Experimental study of Rayleigh-Taylor instability: Low Atwood number liquid systems with single-mode initial perturbations. *Physics of Fluids*, 13(5):1263–1273, 2001. 12
- [36] J. Von Neumann and R. D. Richtmyer. A method for the numerical calculation of hydrodynamic shocks. *J. Appl. Phys.*, 21:232–237, 1950. 1.1